Original

Luminescence, structure and insight on the inversion degree from normal to inverse spinel in a ZnAl$_{(2-x)}$Fe$_x{}^{3+}$O$_4$ system

Simon N. Ogugua [a,*], *Odireleng M. Ntwaeaborwa* [b], *Hendrik C. Swart* [a]

[a] *Department of Physics, University of the Free State, Bloemfontein ZA-9300, South Africa*
[b] *School of Physics, University of the Witwatersrand, Private Bag 3, Wits 2050, South Africa*

ABSTRACT

ZnAl$_2$O$_4$ doped with various concentration (x) of Fe^{3+} were prepared using the Pechini synthesis. In the first set of samples, Fe^{3+} substituted Al^{3+} to create a system of the form ZnAl$_{(2-x)}$Fe$_x{}^{3+}$O$_4$ ($x=0$–0.08). To study the effect of charge compensation, Fe^{3+} substituted Zn^{2+} to create Zn$_{(1-x)}$Fe$_x{}^{3+}$Al$_2$O$_4$ ($x=0.05$) system. The structure and particle morphology of the phosphors were studied using X-ray diffractometer (XRD) and field emission scanning electron spectroscopy, respectively. From the XRD data, the oxygen parameter and the inversion degrees were estimated. The elemental composition and electronic states of the phosphors were analyzed using X-ray photoelectron spectroscopy (XPS). XPS results showed that part of the Fe^{3+} were reduced to Fe^{2+} in the doped samples. Both photoluminescence and cathodoluminescence properties of the phosphors were also studied. Luminescence excitations using a xenon lamp and X-ray showed two broad emission bands located around 470 and 730 nm, and were ascribed to Fe ions occupying the tetrahedral (tet) and the octahedral (oct) sites in ZnAl$_2$O$_4$, respectively. A change in the lifetime of these two emission bands upon Fe doping further confirmed the existence of Fe in the tet and oct sites in the ZnAl$_{(2-x)}$Fe$_x{}^{3+}$O$_4$ matrix.

© 2020 SECV. Published by Elsevier España, S.L.U. This is an open access article under the CC BY-NC-ND license (http://creativecommons.org/licenses/by-nc-nd/4.0/).

Luminiscencia, estructura e información sobre el grado de inversión de la espinela normal a la inversa en un sistema ZnAl$_{(2-x)}$Fe$_x{}^{3+}$O$_4$

RESUMEN

Se preparó ZnAl$_2$O$_4$ dopado con varias concentraciones (x) de Fe^{3+} usando la síntesis de Pechini. En el primer conjunto de muestras, Fe^{3+} sustituyó Al^{3+} para crear un sistema de la forma ZnAl$_{(2-x)}$Fe$_x{}^{3+}$O$_4$ ($x=0$ a 0,08). Para estudiar el efecto de la compensación de carga, Fe^{3+} sustituyó Zn^{2+} para crear el sistema Zn$_{(1-x)}$Fe$_x{}^{3+}$Al$_2$O$_4$ ($x=0,05$). La estructura y la morfología de las partículas de los fósforos se estudiaron utilizando

* *Corresponding author.*
E-mail address: Oguason@yahoo.com (S.N. Ogugua).

un difractómetro de rayos X (XRD) y espectroscopía electrónica de barrido de emisión de campo, respectivamente. A partir de los datos XRD se estimaron el parámetro de oxígeno y los grados de inversión. La composición elemental y los estados electrónicos de los fósforos se analizaron mediante espectroscopía de fotoelectrones de rayos X (XPS). Los resultados de XPS mostraron que parte de Fe^{3+} se redujo a Fe^{2+} en las muestras dopadas. También se estudiaron las propiedades de fotoluminiscencia y catodoluminiscencia de los fósforos. Las excitaciones de luminiscencia usando una lámpara de xenón y rayos X mostraron dos amplias bandas de emisión ubicadas alrededor de 470 y 730 nm, y se atribuyeron a iones Fe que ocupan los sitios tetraédricos (tet) y octaédrico (oct) en $ZnAl_2O_4$, respectivamente. Un cambio en la vida útil de estas dos bandas de emisión después del dopaje con Fe confirmó aún más la existencia de Fe en los sitios tet y oct en la matriz $ZnAl_{(2-x)}Fe_x^{3+}O_4$.

Introduction

A spinel unit cell contains 8 face-centered cubics (FCC) cells. Spinels are made up of an anion, occupying the FCC lattice points, forming octahedral (oct) and tetrahedral (tet) sites with two central metal ions, usually divalent and trivalent ions, respectively [1]. They are represented by a general formula AB_2O_4, where "A^{2+}" is a divalent metal ion occupying the tet sites and "B^{3+}" is a trivalent metal ion occupying the oct sites. Spinels belong to the $F-d3m$ space group. Each unit cell contains 32 oxygen (O^{2-}) atoms, with 8 "A^{2+}" atoms and 16 "B^{3+}" atoms. Depending on the distribution of the "A^{2+}" and "B^{3+}" ions in the unit cell, spinels are divided into normal and inverse. Normal spinels have a cubic closed-packed (ccp) structure with more "B^{3+}" ions than "A^{2+}" ions. The "A^{2+}" ions occupying $^1/_8$ of the tet sites and the "B^{3+}" ions occupying ½ of the oct sites. Atomic arrangement in the inverse spinel is such that the whole A^{2+} ions and ½ of the B^{3+} ions occupy the oct sites, while the other ½ of the B^{3+} ions occupy the tet sites. Furthermore, there is an intermediate structural arrangement described by the formula $(A_{1-y}B_y)[A_{y/2}B_{1-y/2}]_2O_4$ with the terms in parentheses and square brackets denoting the tet and oct sites, respectively. y is called the inversion degree, and its values range from 0, for normal structure, and 1, for inverse structure, and $^2/_3$ for random ion distribution [2].

$ZnAl_2O_4$ belong to the spinel group known as the spinel-aluminate family. It is naturally available in a mineral called gahnite. $ZnAl_2O_4$ has almost normal spinel structure [3]. Like other normal spinel structures, $ZnAl_2O_4$ has cubic symmetry, $Fd-3m$ space group and 8 formulae per unit cell [4]. The O^{2-} ions form a closed-packed structure with 64 tet and 32 oct interstices per unit cell. As mentions previously, only $^1/_8$ of the tet voids are occupied by Zn^{2+}, while the Al^{3+} occupies half (½) of the oct voids. Generally, in one FCC unit cell, the effectual number of ions occupying the lattice point is 4 [5]. Concurrently, the effectual number of ions in the oct and tet voids are 4 and 8, respectively. Hence, in $ZnAl_2O_4$, Zn^{2+} ions occupy $8 \times {}^1/_8 \times 8 = 8$ tet sites of T_d symmetry and Al^{3+} ions occupy $8 \times ½ \times 4 = 16$ oct sites of D_{3d} symmetry; while O^{2-} ions occupy $8 \times 4 = 32$ sites of C_{3v} symmetry [6]. Fig. 1(a) shows the schematic illustrations of the $ZnAl_2O_4$ unit cell with only five oct and seven tet sites. Fig. 1(b) and (c) shows the coordinates of the tet site and the oct site, respectively.
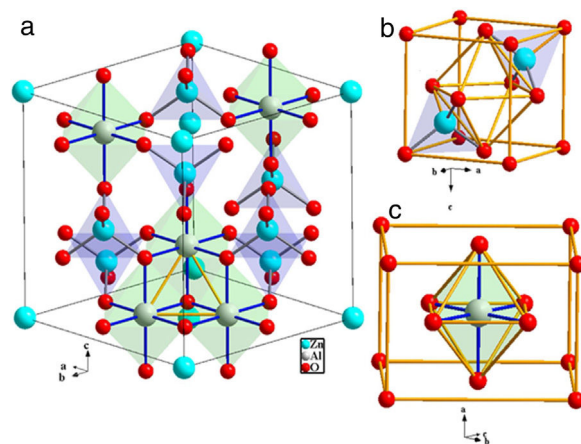
Fig. 1 – Diagrammatic illustration of the $ZnAl_2O_4$ spinel structure showing; (a) a unit cell with five oct sites (mint green) and seven tet sites (lilac blue), (b) double tet and (c) oct coordinates.

Transition-metals have edge over rare earth elements from an economic point of view [7,8]. They have the capacity to give broadband emission in the visible and infrared regions [2,8–11], which leads to their aptness in tunable radiation sources in optical devices [12–15]. In particular, Fe^{3+} doped matrices are of special importance due to its ability to emit in lower and higher wavelength ends of the visible spectrum when doped into tet and oct sites, respectively [2,16].

Electrical neutrality can be maintained in a solid material through charge balance. Charge imbalance can lead to the formation of charge defects in the host lattice and hence creates non-radiative luminescence centers in the material [17]. The presence of non-radiative transitions, largely, can reduce the luminescence emission intensity and hence luminescence efficiency of a phosphor [18]. Different charge compensation models have been used in enhancing the luminescence of phosphors [17,19–21]. The first model involves a divalent ion replaced by a trivalent ion. In this model, the host has to capture one O_2 from the air to balance the charge differently. The second model involves replacement of three divalent ions by two trivalent ions, with the charge balance contributed by the extra vacancy provided by the excess divalent ion. In the

third model, two divalent ions are replaced by one trivalent ion and one alkali metal ion (monovalent ion) is used to balance the charge. The relative intensities of the phosphors prepared using the second and third model was found to be twice that of the phosphor prepared using the first [20].

In different instances, researchers have reported $ZnAl_2O_4$ doped trivalent metal ions (Dy^{3+}, Eu^{3+}, Td^{3+}, Fe^{3+}, Fe^{3+}, Ce^{3+}), while substituting the trivalent metal ions in the place of Zn^{2+}, without considering the consequences of charge imbalance on the luminescence properties [1,2,22,23]. Hence, in this report, the luminescent properties of $Zn_{(1-x)}Fe_x^{3+}Al_2O_4$ and $ZnAl_{(2-x)}Fe_x^{3+}O_4$ ($x = 0$, 0.01, 0.025, 0.05, 0.08) matrices were studied. In the $Zn_{(1-x)}Fe_x^{3+}Al_2O_4$ system, one Zn^{2+} ion was substituted by one Fe^{3+} ion. Because of the charge imbalance in this system, the host has to trap ambient O_2 to compensate for charge. In the $ZnAl_{(2-x)}Fe_x^{3+}O_4$ system, one Al^{3+} ion was substituted by one Fe^{3+} ion ensuring direct charge balance system.

Experimental

Synthesis

$ZnAl_2O_4$ doped with different mol% of Fe^{3+} were synthesized using the Pechini synthesis method. The starting materials were zinc nitrate hexahydrate ($Zn(NO_3)_2 \cdot 6H_2O$), aluminum nitrate nonahydrate ($Al(NO_3)_3 \cdot 9H_2O$), iron nitrate nonahydrate ($Fe(NO_3)_3 \cdot 9H_2O$), tartaric acid ($C_4H_6O_6$) and nitric acid. For the undoped sample, 3.245 and 8.184 g mass of $Zn(NO_3)_2 \cdot 6H_2O$, and $Al(NO_3)_3 \cdot 9H_2O$, respectively, were dissolved in 10 mL of nitric acid in a glass beaker, and it was labeled solution "A". 6.549 g of $C_4H_6O_6$ was dissolved in 40 mL of distilled water in a different glass beaker, and it was labeled solution "B". Solutions "A" and "B" were stirred using different magnetic stirrers on a hot plate set at 150 °C for about 20 min until transparent solutions were obtained. The two transparent solutions were combined and the mixture was stirred at 150 °C temperature for about 2 h until the liquid evaporated. Prior to the end of the reaction, an evolution of a brownish fume was observed. Still, inside the glass beaker, the sample was dried at 80 °C for 10 h to get white powder. After grinding the sample with an agate mortar and a pestle, it was calcined at 600 °C for 3 h. For the doped samples, different amount of $Fe(NO_3)_3 \cdot 9H_2O$ (0.0008, 0.0022, 0.0044, 0.0071 g) were added to substitute $Al(NO_3)_3 \cdot 9H_2O$ and create matrices of the form $ZnAl_{(2-x)}Fe_x^{3+}O_4$ ($x = 0.01$, 0.025, 0.05, 0.08). A matrix of the form $Zn_{(1-x)}Fe_x^{3+}Al_2O_4$ ($x = 0.05$) was also created by substituting $Zn(NO_3)_2 \cdot 6H_2O$ with 0.0022 g of $Fe(NO_3)_3 \cdot 9H_2O$, the aforementioned procedure was repeated.

Characterization

A Bruker D8 Advanced X-ray diffractometer (XRD) using monochromatic Cu Kα ($\lambda = 1.5406$ Å) X-ray as radiation source was used to characterize the structure of the materials. The morphologies and the elemental analysis of the powders were studied using a JEOL JSM-7800F field emission scanning electron microscope (FE-SEM) fitted with Oxford X-Max^N 80 energy-dispersive X-ray spectrometer (EDS). A PHI 5000

Table 1 – The ionic radii of Zn^{2+}, Al^{3+}, Fe^{3+} and Fe^{2+} in the tet and oct coordinates.

Ions	Tet ionic radius (nm)	Oct ionic radius (nm)	Ref.
Zn^{2+}	0.06	0.074	
Al^{3+}	0.039	0.054	[26]
Fe^{3+}	0.049	0.065	
Fe^{2+}	0.063	0.078	

Table 2 – Estimated crystallite sizes and strain of $ZnAl_{(2-x)}Fe_x^{3+}O_4$ ($x = 0$, 0.01, 0.025, 0.05, 0.08) phosphors.

$ZnAl_{(2-x)}Fe_x^{3+}O_4$	Crystallite size (L) (nm)	Strain (ε) $\times e^{-4}$
$x = 0$	27.8	10.8
$x = 0.01$	33.5	11.2
$x = 0.025$	41.8	14.7
$x = 0.05$	80.6	17.6
$x = 0.08$	86.6	17.6

Versaprobe-scanning ESCA microprobe X-ray photoelectron spectroscopy (XPS) was used to obtain the chemical and electronic state data of the samples. A PerkinElmer Lambda 950 UV-Vis spectrometer was used to record the ultraviolet–visible (UV–vis) diffuse reflectance data. An FLS980 fluorescence spectrometer-(Edinburgh Instruments) fitted with a 450 W Xenon lamp as a source of steady-state excitation was used to collect the PL data.

Results and discussion

Fig. 2(a) shows the XRD patterns of $ZnAl_{(2-x)}Fe_x^{3+}O_4$ ($x = 0$, 0.01, 0.025, 0.05, 0.08) compared to the standard phase of $ZnAl_2O_4$, referenced in JCPDS file no. 82-1043. All the samples show identical patterns as the standard data of spinel $ZnAl_2O_4$, indicating that they crystallized in a single-phase cubic symmetry and $Fd3m$ space group of $ZnAl_2O_4$. Fig. 2(b) shows the XRD pattern in the diffraction angle range of 36.6–37.6 (2θ), depicting the (3 1 1) diffraction plane. It is seen from Fig. 2(b) that the (3 1 1) peak shifted to the lower diffraction angle relative to the undoped sample with increasing Fe^{3+} [24,25]. The shift may be due to distortions in the $ZnAl_2O_4$ host lattices since the dopant (Fe^{3+}) have larger ionic radius than Al^{3+} (see Table 1) [26].

The average crystallite size (L) of the phosphors is related to its lattice strain (ε) by Williamson–Hall equation [27,28] given by Eq. (1):

$$\beta_{hkl} \, Cos \, \theta = \frac{\kappa \lambda}{L} + 4\varepsilon \, Sin \, \theta \qquad (1)$$

where β_{hkl} is the full width at half maximum (FWHM) of each diffraction peak, λ is the wavelength of the X-ray (0.15406 nm) used for measurement, θ is the Bragg angle and κ is a constant related to the crystallite shape, taken as 0.9 for spherical crystals. From a graph of $\beta_{hkl} \, Cos \, \theta$ versus $4 \, Sin \, \theta$, the crystallite size and the strain were determined from the y-intercept and the slope of the graph, respectively. The estimated values of the crystallite sizes and the strain for the undoped sample and for the samples doped with different concentration of Fe^{3+} are listed in Table 2. It is evident from Table 2 that the crystallite size and the strain increased with the Fe^{3+} concentration.
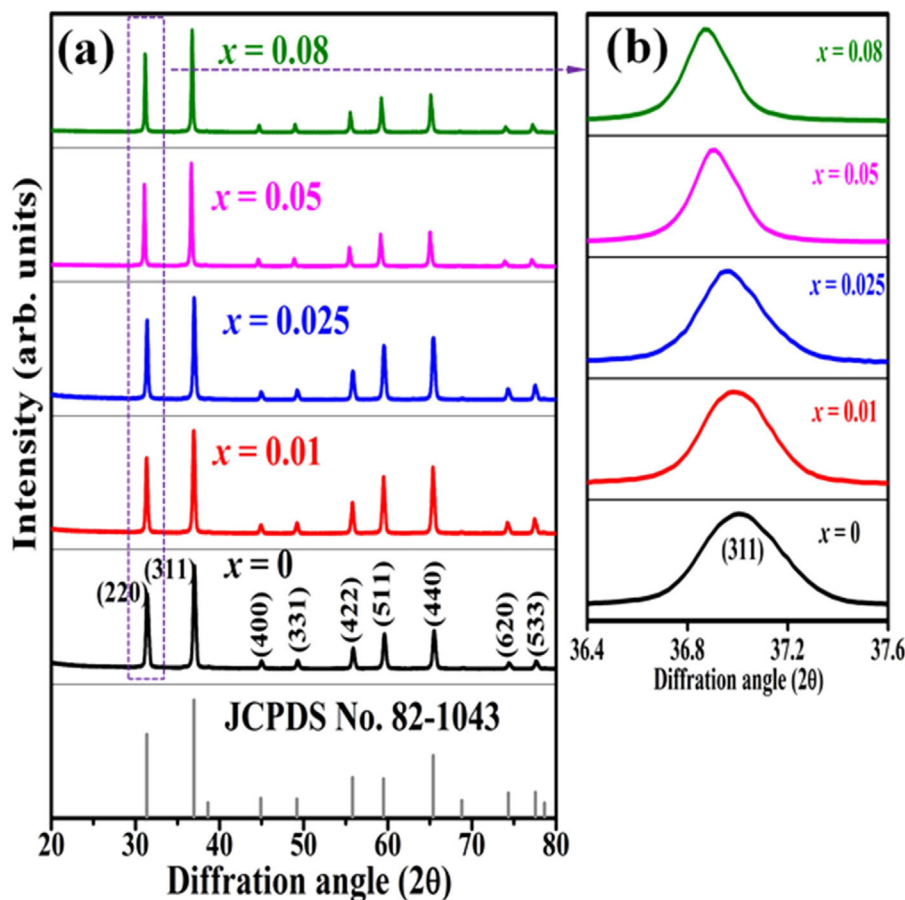
Fig. 2 – The XRD patterns of $ZnAl_{(2-x)}Fe_x^{3+}O_4$ ($x = 0$, 0.01, 0.025, 0.05 and 0.08) and the JCPDS standard.

The lattice constant (lattice parameter) defines the physical dimension of a unit cells in a crystal lattice. For a cubic crystal, the lattice parameter (a) (the length of the edges of the unit cells), the interplanar spacing (d) (the perpendicular distance between successive parallel planes of the atoms in a crystal), and the Miller indices (hkl) (notations for planes in crystal lattices) are related by Eq. (2) [29]:

$$a^2 = d^2(h^2 + k^2 + l^2) \tag{2}$$

The d is related to the X-ray wavelength (λ) and the diffraction angle (θ) by Eq. (2):

$$d = \frac{\lambda}{2\,Sin\,\theta} \tag{3}$$

Hence, the values of 'a' and 'b' can be calculated using Eqs. (2) and (3) and the value of the 'θ' can be determined from the XRD data. The calculated values of a are listed in Table 2. In spite of having cubic symmetry, spinels structures cannot be explained entirely by the lattice parameters (a). An additional dimensionless parameter (oxygen parameter, u) is used to define the slight distortion that occur in the FCC oxygen lattice for a complete description of the spinel lattice points [30]. For an undistorted oxygen lattice in spinels, $u = 0.250$ if the origin of the unit cell is taken at the center of symmetry. The oxygen parameter, u, the lattice parameter, a, and the

cation-anion distance in the tet and oct sites (R_{tet} and R_{oct}, respectively) are related by Eqs. (4) and (5) [31]:

$$R_{tet} = a\sqrt{3}\left(u - \frac{1}{8}\right) \tag{4}$$

$$R_{oct} = a\left(3u^2 - 2u + \frac{13}{8}\right)^{1/2} \tag{5}$$

Inasmuch as a and u give information about the lattice positions, for an absolute representation of the spinel lattice, the proportion of cations occupying the different sites should be determined. The distribution parameter (y) is the degree of inversion and it defines the fraction of the trivalent ions occupying the tet sites. Hence, it varies from 0 to 1 for totally normal and inverse spinels, respectively. Eqs. (4) and (5) are valid for only "perfect" normal or inverse spinels. The distribution of cations in the sites of normal spinels such as gahnite, $ZnAl_2O_4$, is represented by formula {1}:

$$(Zn_8{}^{2+})_{tet}[Al_{16}{}^{3+}]_{oct}O_{32} \tag{1}$$

with the divalent cations, Zn^{2+}, occupying the tet sites (tet) and the trivalent cations, Al^{3+}, occupying the oct sites [30]. Doping $ZnAl_2O_4$ with different concentrations Fe^{3+} will result in the formation of $ZnAl_{(2-x)}Fe_x^{3+}O_4$ composite, resulting in the creation of some Fe–O–Fe bonds in the matrix. This may lead to

the formation of some spinel ferrites ($ZnFe_2O_4$), which have similar structure as $ZnAl_2O_4$, within the matrix [32]. Furthermore, some of the Fe^{3+} can be reduced to Fe^{2+} as confirmed by the XPS result (Fig. 8(a)) via the equation $Fe^{3+} + e^- \rightarrow Fe^{2+}$ [33,34], resulting in the formation of iron oxides, such as Fe_3O_4 (magnetite) within the $ZnAl_{(2-x)}Fe_x{}^{3+}O_4$ matrix. The existence of Fe^{2+} in the matrices indicates that $ZnAl_{(2-x)}Fe_x{}^{3+}O_4$ does not crystallize in a pure normal spinel phase, rather it crystallized as a mixture of normal and inverse spinel, since Fe_3O_4 crystallizes in an inverse spinel. In inverse spinels, such as magnetite, Fe_3O_4, the distribution of the cations in the sites are represented by formula {2}:

$$(Fe_8{}^{3+})_{tet}[F_8{}^{3+}F_8{}^{2+}]_{oct}O_{32} \qquad [2]$$

with one-half of the trivalent cations, Fe^{3+}, occupying the tet sites, while both the divalent cations, Fe^{2+}, and the remaining Fe^{3+} share the oct sites [30].

Furthermore, a solid solution formed by $ZnAl_{(2-x)}Fe_x{}^{3+}O_4$ and Fe_3O_4 is represented by formula {3}, by combining formula {1} and {2}, bearing in mind that Zn^{2+} and Fe^{3+} prefer the tet site in $ZnAl_2O_4$ and Fe_3O_4, respectively.

$$(Zn_{8-x}{}^{2+}Fe_x{}^{3+})_{tet}[Al_{8-x}{}^{3+}Fe_x{}^{3+}F_8{}^{2+}]_{oct}O_{32} \qquad [3]$$
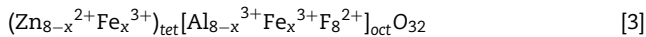
In formula {3}, we assumed that $ZnAl_2O_4$ and $ZnFe_2O_4$ have similar structure (normal spinels), and hence the combination of the two compounds should not have substantial effect on the spinel type. Formula {3} will form a solid solution with properties lying between normal and inverse spinels. In the case where more than one cation occupies the same site, the bond length is determined by finding the effective bond length – i.e. the average of the individual cationic bond length [30]. Therefore, for a cation, i with bond length R_i and mole fraction z_i on the tet site the effective bond length is defined by Eq. (6):

$$R_{tet} = \sum_i z_i R_i \qquad (6)$$

also, a similar expression is used for R_{oct}. The bond lengths were determined by combining Eqs. (4)–(6), and substituting the values of u and a for the end members, $ZnAl_2O_4$ and Re_3O_4 from Table 3. Also keeping in mind that the tet sites are completely occupied by Zn^{2+} in $ZnAl_2O_4$ and by Fe^{3+} in Fe_3O_4. The resulting values of the bond lengths are listed in Table 3.

It is seen from formula {3} that Zn^{2+} and Al^{3+} only occupy the tet and oct sites, respectively. Hence, the change of the
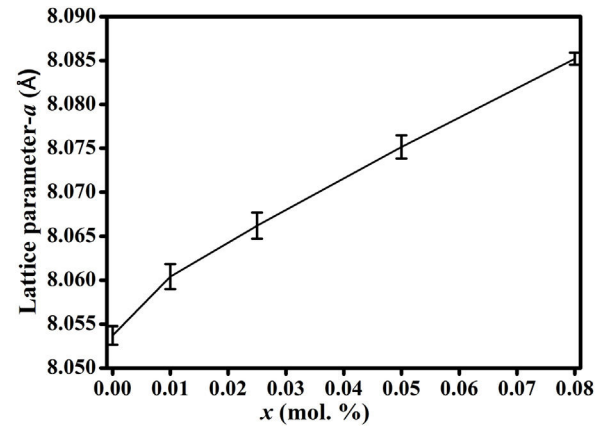

Fig. 3 – A graph of the lattice parameter (*a*) of $ZnAl_{(2-x)}Fe_x{}^{3+}O_4$ (*x* = 0, 0.01, 0.025, 0.05, 0.08) as a function of the Fe^{3+} ion concentration.

crystal structure with the composition of Fe will depend on the distribution of the Fe^{3+} and Fe^{2+} cations in the available tet and oct sites, respectively. In additions, a varies linearly with the dopant concentration (x) (see Fig. 3), hence, the distribution of Fe^{2+} and Fe^{3+} varies linearly within the crystal. For y fraction of Fe^{3+} and Fe^{2+} occupying the tet and oct sites, respectively, R_{tet} and R_{oct} are given by Eqs. (7) and (8), respectively, for the sample with $x = 0.01$.

$$R_{tet} = 0.99R_{Zn^{2+},tet} + yR_{Fe^{3+},tet} + (0.01 - y)R_{Fe^{2+},tet} \qquad (7)$$

$$R_{oct} = \frac{1.99R_{Al^{3+},oct} + (0.01 - y)R_{Fe^{3+},oct} + yR_{Fe^{2+},oct}}{2} \qquad (8)$$

By equating Eqs. (4) and (5) to Eqs. (7) and (8), respectively, and substituting the values of the bond lengths R and the lattice parameters a, the values of y and u can be determined. Following the same procedure, the value of y and u is determined for the rest of the samples, and the results are presented in Table 4.

The FE-SEM images of the undoped and 0.08 mol% Fe^{3+} doped $ZnAl_2O_4$ are shown in Fig. 4(a) and (b), respectively. Fe^{3+} doping showed no significant effect on the morphologies of the phosphors. Both images show agglomerated spherical grains with what appear to be distinctive grain boundaries and varying grain sizes. The average diameters of the particles were taken randomly using the line tool in the ImageJ software, version IJ 1.46r [37]. The size distribution curves were

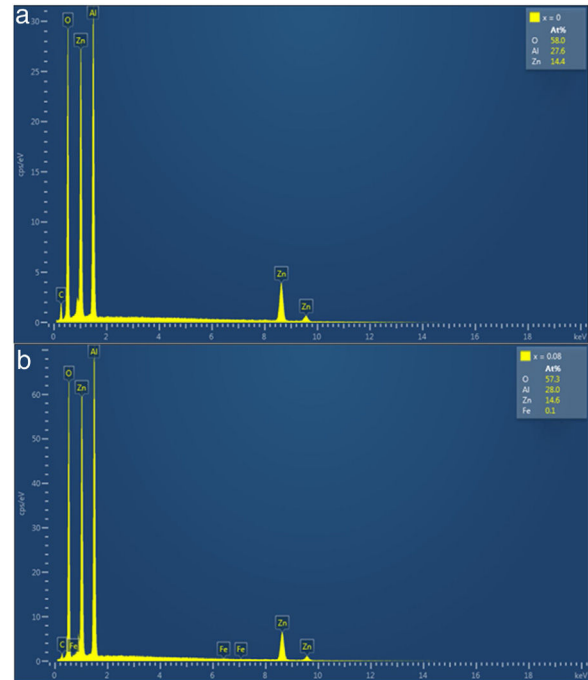| Table 3 – The lattice parameters and inversion degree of different spinel composition.					
X	a (Å)	u (literature)	u (calculated)	y (literature)	y (calculated)
0	8.054 ± 0.001	0.261*	–	0.00*	–
0.01	8.060 ± 0.001	–	0.261	–	0.04
0.025	8.066 ± 0.001	–	0.262	–	0.08
0.05	8.075 ± 0.001	–	0.262	–	0.11
0.08	8.085 ± 0.001	–	0.262	–	0.15
Fe_3O_4	8.392*	0.255*	–	1.00*	–
* [30].					

Table 4 – Calculated bond lengths of the cations-O in ZnAl$_{(2-x)}$Fe$_x^{3+}$O$_4$ system in the tet and oct sites compared to the literatures.

Cation	R_{tet} (calculated)	R_{tet} (literature)	R_{oct} (calculated)	R_{oct} (literature)
Zn^{2+}	1.8971	1.9493[**]	–	–
Fe^{2+}	–	1.9950[*]	2.0996	2.0800[***]
Fe^{3+}	1.8867	–	2.0175	2.0300[***]
Al^{3+}	–	–	1.9289	1.9169[**]

* [30].
** [35].
*** [36].
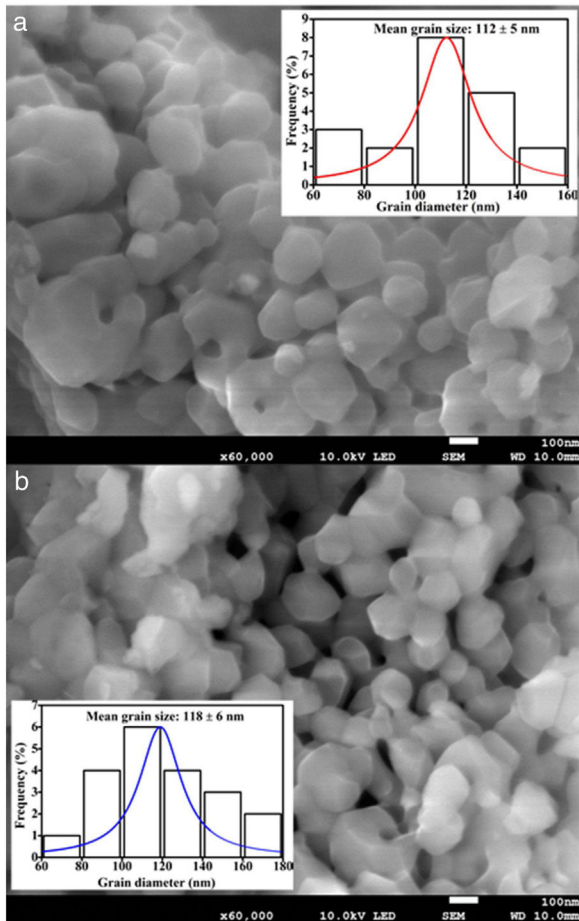
Fig. 4 – The FE-SEM images of ZnAl$_{(2-x)}$Fe$_x^{3+}$O$_4$ (a) $x = 0$ and (b) $x = 0.08$. The inset of (a) and (b) depicts the average particle size distribution curves for the images thereof.

Fig. 5 – The EDS spectra of ZnAl$_{(2-x)}$Fe$_x^{3+}$O$_4$ (a) $x = 0$ and (b) $x = 0.08$. The inset of (a) and (b) are the at.% elemental concentration.

obtained from the FE-SEM images, with estimated mean grain sizes of 112 ± 5 and 118 ± 6 nm for the undoped and 0.08 mol% Fe^{3+} doped ZnAl$_2$O$_4$ as shown in the insets of Fig. 4(a) and (b), respectively. The estimated grain sizes for the samples doped with other mol% of Fe^{3+} ($x = 0.01$, 0.025, 0.05, 0.08) were 115, 117, 124 and 128 nm, respectively. Compared to the crystallite size obtained from the XRD data, the grain size is much bigger. Wang, Li, and Tamrakar et al. have reported similar result [38–40]. The grain size and the crystallite size of the particles are different owing to the formation of polycrystalline

aggregates [41], which appears as one particle in SEM, especially in amorphous materials [39].

The EDS was used for the semiquantitative and the elemental composition analysis of ZnAl$_{(2-x)}$Fe$_x^{3+}$O$_4$, $x = 0$–0.08 phosphors and the spectra for $x = 0$ and 0.08 are shown in Fig. 5(a) and (b), respectively. The elements (Zn, Al and O) expected in the compounds are present in the EDS spectra of the all samples. In the doped samples, 0.1 at.% of Fe was observed in the samples with high concentration of Fe ($x = 0.05$ and 0.08). The same amount of Fe was measured in the EDS spectra of the samples, even though they contain different concentration of Fe. This could be due to the detection limit of the technique $\sim 0.1\%$ [42]. This imply that measured values of 0.05 and 0.14% should be approximated to 0.1%. The presence of carbon (C) in the EDS spectra could be from environmental hydrocarbon and/or carbon tape on which the samples were mounted. The insets of Fig. 5(a) and (b) are the measured elemental concentration at.% of all the elements present in the ZnAl$_{(2-x)}$Fe$_x^{3+}$O$_4$, $x = 0$ and 0.08 samples, and Table 5

Table 5 – Elemental composition and concentration ZnAl$_{(2-x)}$Fe$_x{}^{3+}$O$_4$ phosphors ($x=0$, 0.01, 0.025, 0.05 and 0.08).

Samples	Elements/compositions (at.%)			
ZnAl$_{(2-x)}$Fe$_x{}^{3+}$O$_4$	Zn	Al	O	Fe
$x=0$	14.4	27.6	58.0	0
$x=0.01$	14.5	28.0	57.5	0
$x=0.025$	14.6	28.3	57.1	0
$x=0.05$	14.6	28.2	57.1	0.1
$x=0.08$	14.6	28.0	57.3	0.1

presents the elemental concentration at.% present in the ZnAl$_{(2-x)}$Fe$_x{}^{3+}$O$_4$ ($x=0$, 0.01, 0.025, 0.05 and 0.08) phosphors.

XPS is an in situ technique where a specimen is irradiated with X-rays leading to ionization, and ejection of photoelectrons from the core-shell and the kinetic energies distribution are measured using electron energy analyzer and a photoelectron spectrum can thus be recorded [43]. XPS was used to determine the electronic and chemical bonding state from the surface of the samples. The XPS spectra were fitted using the PHI MULTIPAK software, version 8.2C [44].

Fig. 6(a)–(d) shows, respectively, the fitted high-resolution O 1s XPS spectra of ZnAl$_{(2-x)}$Fe$_x{}^{3+}$O$_4$ for $x=0$, 0.01, 0.05 and 0.08. The spectra show two peaks for the undoped ZnAl$_2$O$_4$ sample ($x=0$, Fig. 6(a)), but exhibits three peaks for the Fe^{3+} doped samples ($x=0.01$, 0.05 and 0.08, Fig. 6(b–d)). The two components centered at 531.3 and 533.0 eV in Fig. 6(a) are ascribed to the metal–oxygen (M–O) bonds [45] and O–H bonds from water molecules absorbed from the environmental moisture, respectively [46,47]. The additional peak centered at 534.1 eV for $x=0.01$ and 534.0 eV for $x=0.05$ and 0.08 is ascribed to the Fe–OH bonds [48]. This indicates that Fe ions were incorporated successfully into the ZnAl$_2$O$_4$ host. The peaks belonging to M–O and O–H bonds in Fig. 6(a)–(d) shifted slightly to lower binding energy after Fe^{3+} doping.

The Al 2p high-resolution XPS spectra for ZnAl$_{(2-x)}$Fe$_x{}^{3+}$O$_4$ ($x=0$, 0.01, 0.05 and 0.08), are shown, respectively, in Fig. 7(a)–(d). The two peaks centered at 74.2 and 75.1 eV in Fig. 7(a) were ascribed to Al ions occupying the tet and oct sites by Tshabalala et al. [49], in comparison with a report on Y$_3$Al$_5$O$_{12}$ (YAG) by Pawlak et al. [50]. However, YAG has an entirely different structure from ZnAl$_2$O$_4$. In the ZnAl$_2$O$_4$ system, the tet sites is occupied by only Zn^{2+} ions and the oct sites is occupied by only Al^{3+} ions [30] as shown in Fig. 1 and by formula {1}, while in YAG, Al^{3+} ions can occupy both tet and oct sites [50]. Furthermore, similar XPS peaks have been observed in doped Al$_2$O$_3$ samples and where assigned to M–Al–O or M–Al (M = metal ion) [51–55]. For instance, in the La$_{1-x}$Al$_x$O$_3$ system, it was assigned to La–Al–O by Fei et al. [51], while in the Ru/La(x)–Al$_2$O$_3$ system, it was assigned to
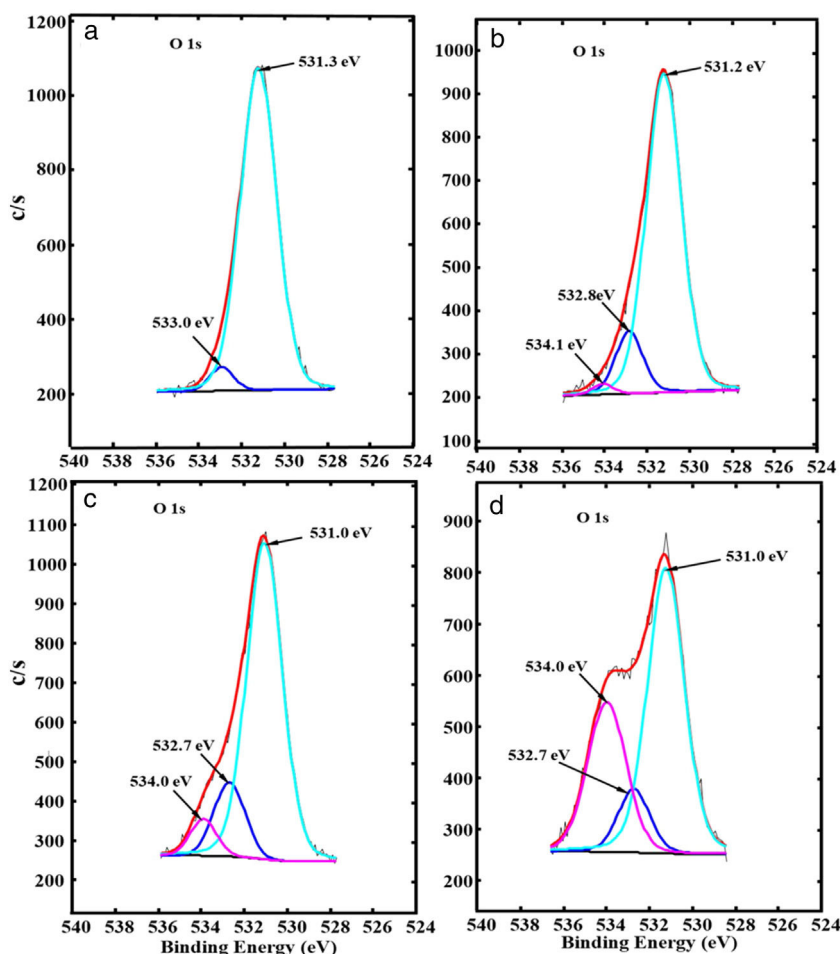

Fig. 6 – The fitted high-resolution O 1s XPS spectra of ZnAl$_{(2-x)}$Fe$_x{}^{3+}$O$_4$, (a) $x=0$, (b) $x=0.01$, (c) $x=0.05$ and (d) $x=0.08$.
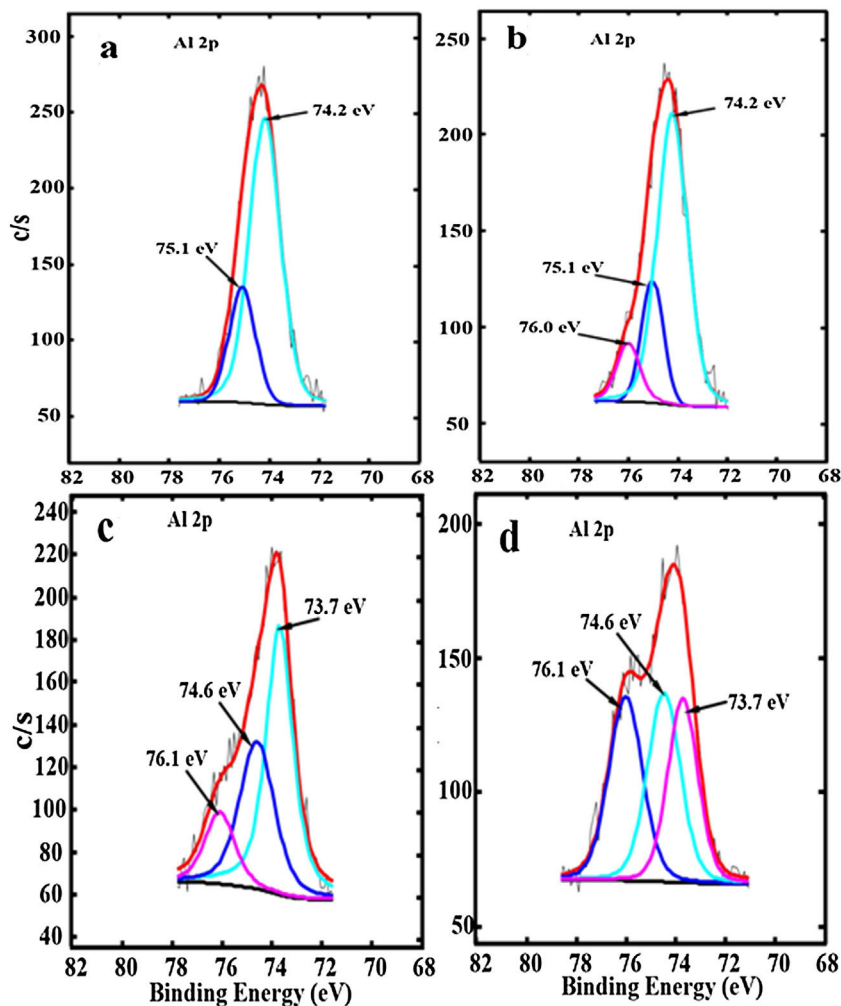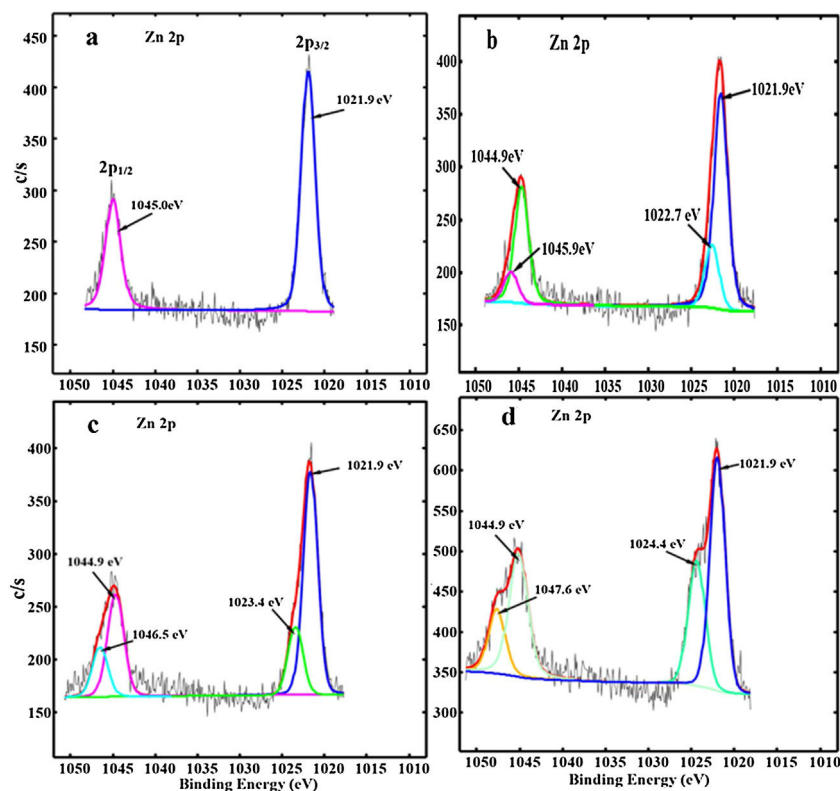
Fig. 7 – The fitted high-resolution Al 2p XPS spectra for ZnAl$_{(2-x)}$Fe$_x^{3+}$O$_4$, (a) $x = 0$, (b) $x = 0.01$, (c) $x = 0.05$ and (d) $x = 0.08$.

Al–La by Chung et al. [52]. Another point that is worth noting is that the peak around 76.0 eV in Fig. 7(b)–(d) (assigned to tet Al by Tshabalala et al. [49]) appears at higher binding energy compare to the other peak (around 74 eV) which they assigned to oct Al. However, it is expected that the higher the number of oxygen coordinating a metal ion, the higher the binding energy since the binding energy increase with electronegativity [56]. Therefore, we believe that the photoelectron peaks at the lower binding energy (74.2 eV) and higher binding energy (75.1 eV) in Fig. 7(a) are due to the Al–O in AlO$_6$ (Al^{3+} ions in the oct sites) [49] and AL–OH [57] in AlO$_6$, respectively. For the Fe^{3+} doped samples, an additional photoelectron peak appeared at the higher binding energy centered at 76.0 eV for the sample doped with 0.01 mol% of Fe^{3+} ($x = 0.01$) and at 76.1 eV for ($x = 0.05$ and 0.08) as shown in Fig. 7(b)–(d). It is also evident from Fig. 7(b)–(d) that the peaks from Al–O and AL–OH shifted to lower binding energies at higher Fe^{3+} doping concentration. The additional peaks observed at 76.0 eV in Fig. 7(b) and at 76.1 eV in Fig. 7(c) and (d), are assigned to the Al–O–Fe at the oct sites, in the ZnAl$_{(2-x)}$Fe$_x^{3+}$O$_4$ system [51,52]. It is interesting to observe that the intensity of the photoelectron peaks from the Al–O–Fe increased with increasing Fe^{3+} concentration, but the intensities of the photoelectron peaks from Al–O

decreased. This shows that more Al–O–Fe are created in the ZnAl$_{(2-x)}$Fe$_x^{3+}$O$_4$ system with increasing Fe^{3+} concentration. The peaks assigned to Al–O–Fe in Fig. 7(b)–(d) appears at higher binding energy with respect to the other peaks assigned to Al–O and AL–OH, because Fe (1.83) have higher electronegativity than Al (1.61) [58].

The deconvoluted Zn 2p XPS spectra for the ZnAl$_{(2-x)}$Fe$_x^{3+}$O$_4$ ($x = 0$, 0.01, 0.05 and 0.08) are shown in Fig. 8(a)–(d), respectively. For the undoped ZnAl$_2$O$_4$ shown in Fig. 8(a), a double peak from the Zn 2p core-level were observed at 1021.9 and 1045.0 eV and are assigned to the Zn 2p$_{3/2}$ and Zn 2p$_{1/2}$ [59] from the Zn occupying the tet site (ZnO$_4$) in ZnAl$_2$O$_4$, respectively. For the Fe^{3+} doped samples (Fig. 8(b–d)), a new photoelectron peak was observed at the higher binding energy with respect to the Zn 2p$_{3/2}$ and Zn 2p$_{1/2}$ peaks which shifted to high binding energy values with increasing Fe^{3+} ions concentration. These peaks are centered at 1022.7 and 1045.9 eV, 1023.4 and 1046.5 eV, 1024.4 and 1047.6 eV for ZnAl$_{(2-x)}$Fe$_x^{3+}$O$_4$ ($x = 0.01$, 0.05 and 0.08), respectively, as shown in Fig. 8(b)–(d) and they are assigned to Zn–O–Fe in the tet sites. Yngman et al. have reported a similar result in Zn doped GaAs [60], Li et al. in Cu doped ZnS [61] and Beltrán et al. in carbon doped ZnO [62].

Fig. 8 – The fitted high-resolution Zn 2p XPS spectra of the ZnAl$_{(2-x)}$Fe$_x^{3+}$O$_4$, (a) $x=0$, (b) $x=0.01$, (c) $x=0.05$ and (d) $x=0.08$.

The peaks assigned to Zn–O–Fe in Fig. 8(b)–(d) appeared at higher binding energy values with respect to the peaks assigned to Zn in ZnO$_4$, because Fe (1.83) have higher electronegativity than Zn (1.65) [58]. However, Zhang et al. [59,63] attributed the photoelectron peaks at the lower binding energies in Zn 2p$_{3/2}$ and Zn 2p$_{1/2}$ to Zn^{2+} ions occupying tet sites and the photoelectron peaks at higher binding energies in Zn 2p$_{3/2}$ and Zn 2p$_{1/2}$ to Zn^{2+} occupying the oct sites in ZnAl$_2$O$_4$:Cr^{3+} system. However, they did not show the XPS spectrum for the undoped ZnAl$_2$O$_4$. In Fig. 8(a), the XPS spectrum for the undoped ZnAl$_2$O$_4$ did not show any sign of the two photoelectron peaks sitting at the higher binding energies with respect to the Zn 2p$_{3/2}$ and Zn 2p$_{1/2}$ peaks. This suggests that the two peaks sitting at higher binding energies to Zn 2p$_{3/2}$ and Zn 2p$_{1/2}$ peaks in Fig. 8(a) are associated with Fe ions. The intensities of the photoelectron peaks from the Zn–O–Fe in Fig. 8(b)–(d) increased as the Fe^{3+} ions concentration increased in ZnAl$_{(2-x)}$Fe$_x^{3+}$O$_4$ system. However, unlike the Al 2p peaks, there was no significant change in the Zn 2p peaks intensities. The formation of Zn–O–Fe and Al–O–Fe bonds in the ZnAl$_2$O$_4$: Fe^{3+} matrices suggest the possibility of existence of tet and oct Fe in these matrices.

The Fe XPS peaks could not be detected in the samples doped with concentration of up to 0.08 mol%, hence we prepared another sample doped with 4 mol% of Fe^{3+}. Fig. 9(a) shows the deconvoluted XPS spectrum for Fe 2p peak. The spectrum consists of the shake-up peaks (satellite peaks) and the Fe 2p$_{3/2}$ and Fe 2p$_{1/2}$ components. Each component of the Fe 2p peak consist of two Fe ion peaks signifying the different oxidation states of Fe ion (Fe^{2+} and Fe^{3+}). The shape-up

peaks were located relatively at higher binding energies of 713.0 eV and 725.4 eV with respect to the 2p$_{3/2}$ and 2p$_{1/2}$ components, respectively [64,65]. The photoelectron peaks at the lower binding energies (704.6 and 717.6 eV) in the Fe 2p$_{3/2}$ and 2p$_{1/2}$ components were assigned to Fe^{2+}, while the two peaks at the higher binding energies (706.8 and 720.7 eV) in the Fe 2p$_{3/2}$ and 2p$_{1/2}$ components were assigned to Fe^{3+} [64–66]. With the presence of Fe^{2+} in the crystal, Fig. 9b(i–iii) shows the possible structural makeup of the samples. The structure is made up of a mixture of ZnAl$_2$O$_4$ with tet Zn^{2+} and oct Al^{3+} (Fig. 9b(i)), ZnFe$_2$O$_4$ with tet Zn^{2+} and oct Fe^{3+} (Fig. 9b(ii)), and Fe$_3$O$_4$ with tet Fe^{3+} and oct Fe^{2+} or Fe^{3+} (Fig. 9b(ii)).

The UV–vis spectrometer was used to measure the diffuse reflectance of ZnAl$_{(2-x)}$Fe$_x^{3+}$O$_4$ ($x=0$, 0.01, 0.025, 0.05, 0.08) phosphors in the wavelength range of 250–800 nm and the spectra are shown in Fig. 10. The diffuse reflectance spectra show the ZnAl$_2$O$_4$ band-to-band transition around 305 nm.

The band gaps of the phosphors were determined from the diffuse reflectance data using the derivative method and Kubelka–Munk function. In the derivative method, the band gap is determined by taking the first derivative, dR/dE, of the diffuse reflectance data and plotting it against the energy E (eV) [67] (the wavelength was converted to energy using the relation, E (eV) $= 1240/\lambda$ (nm)). In general, the absorption coefficient of a material is related to the band gap by

$$(\alpha h\upsilon)^{1/n} = A(h\upsilon - E_g) \tag{9}$$

where h is Planck's constant, υ is the frequency, E_g is the material band gap and n depends on the nature of the transition
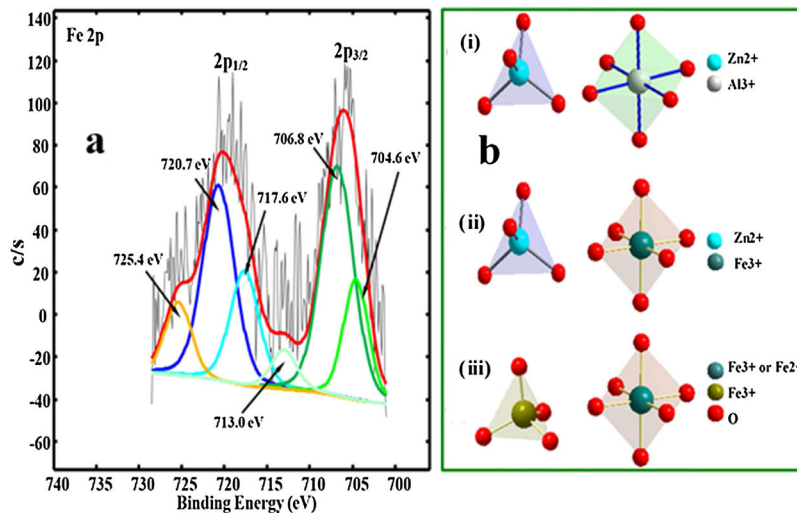
Fig. 9 – (a) The fitted high-resolution Fe 2p XPS spectra of the ZnAl$_2$O$_4$: 4% Fe^{3+}. (b) The structural makeup of ZnAl$_2$O$_4$:Fe^{3+}.
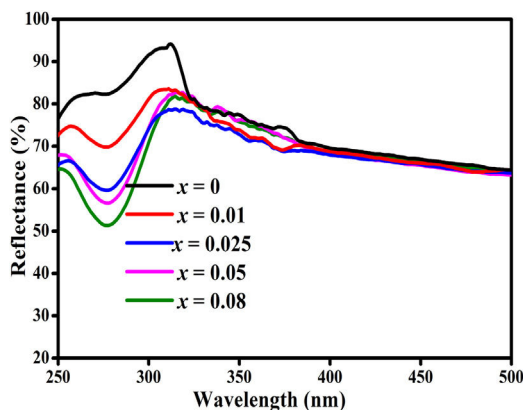

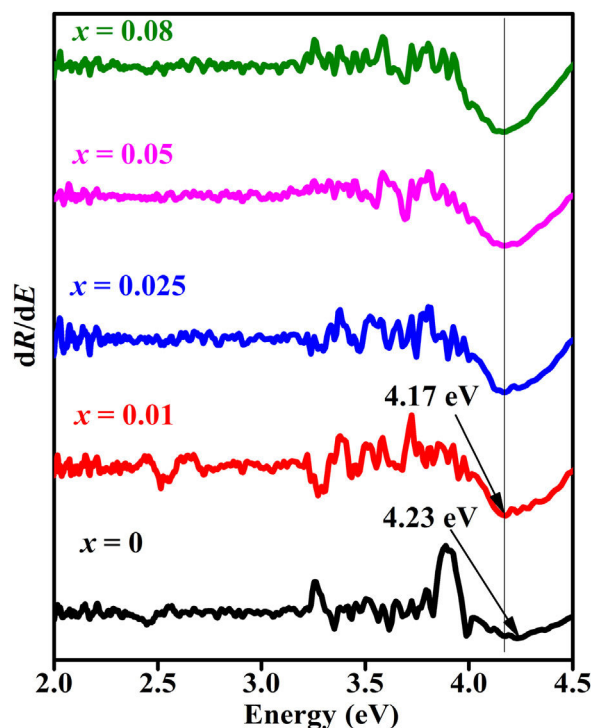Fig. 10 – The diffuse reflectance spectra of ZnAl$_{(2-x)}$Fe$_x^{3+}$O$_4$ (x = 0, 0.01, 0.025, 0.05, 0.08) phosphors.

Fig. 11 – The plots of dR/dE versus E (eV) for the ZnAl$_{(2-x)}$Fe$_x^{3+}$O$_4$ (x = 0, 0.01, 0.025, 0.05, 0.08) phosphors.

and can take values of ½, 3/2, 2 or 3 for allowed direct, forbidden direct, allowed indirect and forbidden indirect transitions, respectively. A is an energy independent proportionality constant [68]. Eq. (9) can be written as:

$$\alpha = \frac{A(h\upsilon - E_g)^n}{h\upsilon} \quad (10)$$

For a direct band gap material, the absorption coefficient is a function of energy, $\alpha(h\upsilon)$, hence Eq. (10) can be expressed as

$$\alpha(h\upsilon) = \frac{A(h\upsilon - E_g)^n}{h\upsilon} \quad (11)$$

Eq. (11) is true for $h\upsilon > E_g$ but 0 if $h\upsilon < E_g$. Taking the first derivative of Eq. (11) with respect to $h\upsilon$ gives

$$\frac{d\alpha(h\upsilon)}{d(h\upsilon)} = \left[\frac{A}{h\upsilon}\left[-\frac{(h\upsilon - E_g)^n}{h\upsilon} + n(h\upsilon - E_g)^{n-1}\right]\quad h\upsilon > E_g\right] \quad (12)$$

Eq. (12) diverges at a point when $hc/E = hc/E_g$, and this correspond to the band gap of a direct band gap material. At this point Eq. (12) is reduce to

$$\frac{d\alpha(h\upsilon)}{d(h\upsilon)}\bigg|_{E=E_g} \to \infty \quad n = 1/2 \quad (13)$$

For a direct band gap material, Eq. (13) show a distinct sharp peak, usually taken as the band gap of the material [67]. Fig. 11 shows the plots of dR/dE versus E (eV) for the ZnAl$_{(2-x)}$Fe$_x^{3+}$O$_4$

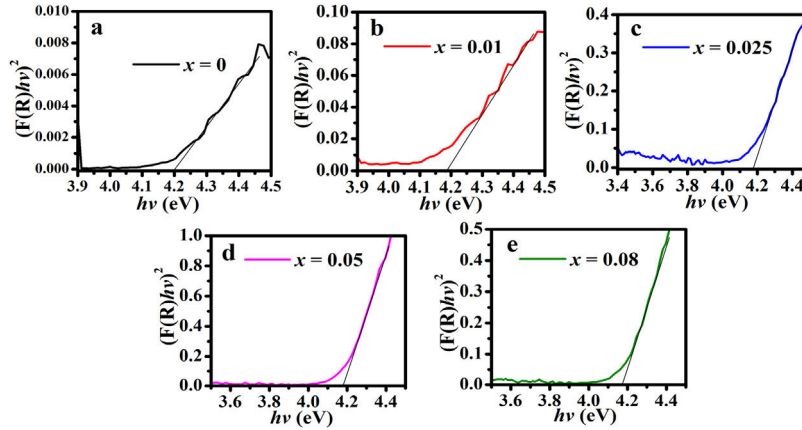Fig. 12 – The plot of $(F(R_{100})h\upsilon)^2$ versus $h\upsilon$ for the $ZnAl_{(2-x)}Fe_x^{3+}O_4$, (a) x = 0, (b) x = 0.01, (c) x = 0.025, (d) x = 0.05, and (e) x = 0.08.

(x = 0, 0.01, 0.025, 0.05, 0.08) phosphors. It is evident from Fig. 11 that the band gap of the undoped $ZnAl_2O_4$ is about 4.23 eV. This is in agreement with some of the $ZnAl_2O_4$ band gap reported in the literature [69,70]. The band gap decreased slightly to 4.17 eV when 0.01 mol% of Fe^{3+} was doped into the matric. This could be due to the smaller band gap of $ZnFe_2O_4$ [71,72] compare to $ZnAl_2O_4$ [69,70]. However, no increased was observe in the band gap for a further increase in the concentration of Fe^{3+}.

The Kubelka–Munk function is based on the direct and indirect proportionality relation between the absorption coefficient (α) of a material and the R, respectively. R is the reflectance of the material. For a semi-infinite medium, Kubelka–Munk is defined by Eq. (14):

$$F(R_\infty) = \left(\frac{(1 - R_\infty)^2}{2R_\infty} \right) \qquad (14)$$

where R_∞ is the reflectance of the semi-finite medium [73]. For a finite medium with 100%, Eq. (14) takes the form of Eq. (15):

$$F(R_{100}) = \left(\frac{(1 - R_{100})^2}{2R_{100}} \right) \qquad (15)$$

Considering that $F(R_\infty)$ is proportional to the α, and equating Eqs. (9) and (15) gives Eq. (16):

$$(F(R_{100})h\upsilon)^{1/n} = A(h\upsilon - E_g) \qquad (16)$$

From Eq. (16), the band gap can be estimated by plotting a graph of $(F(R_{100})h\upsilon)^2$ versus $h\upsilon$ and drawing a straight line from the inflection point of the curve to the $h\upsilon$-axis. Fig. 12 shows the $(F(R_{100})h\upsilon)^2$ versus $h\upsilon$ plot for the $ZnAl_{(2-x)}Fe_x^{3+}O_4$ (x = 0, 0.01, 0.025, 0.05, 0.08) phosphors. Interestingly, the values of the band gaps are in agreement with those estimated with the derivative method, with 4.20 eV for the undoped $ZnAl_2O_4$ and 4.17 eV for all the doped samples.

The non-increment in the band gap with increasing concentration of Fe^{3+} can be explained by Harrison's tight binding (TB) model [74], which proposed that:

(i) The top of the valence band of the host does not change significantly for a small concentration of the dopant and the doped matrix can be adequately explained within the virtual-crystal approximation method.

(ii) The position of the energy of the dopant (impurity) is independent of its concentration (even at the smallest possible concentration). However, at higher concentration, small shifting and broadening of the dopant states may occur (owing to the electrostatic interactions between the dopant atoms and/or the difference in the bond lengths of the host and the dopant within the matrix.

Fig. 13(a) and (b) shows the PL excitation and emission spectra of $ZnAl_{(2-x)}Fe_x^{3+}O_4$ (x = 0, 0.01, 0.025, 0.05, 0.08) phosphors normalized with respect to the dopant concentration, respectively. The excitation spectra (Fig. 13(a)) was obtained when monitoring the emission at 483 nm and scanning the spectrum in the wavelength range of 200–450 nm. Within this wavelength range, two broad bands were observed from 200 to 275 nm, with a maximum at 235 nm, and from 325 to 415 nm, with a maximum around 374 nm. The peak at 235 nm could be due to the band-to-band transition of $ZnAl_2O_4$. The broadband peaking around 374 nm could be relate to ZnO band-to-band transition [75]. Similar transitions were observed from the absorbance and reflectance of the $ZnAl_2O_4$ samples [4,76,77]. Under the 235 nm excitation, two broad emission bands could be distinguished, one with a maximum around 483 nm and the other around 730 nm, as shown in Fig. 13(b).

The inset of Fig. 13(a) shows how the emission intensities of the 487 and 730 nm bands varied with Fe^{3+} concentration. It is apparent from the inset of Fig. 13(a) that the emission intensity of the 487 nm band dropped sharply after doping with just 0.01 mol% of Fe^{3+}, but as the concentration of Fe^{3+} increased, the change in the emission intensity became infinitesimal and intermittent. A similar trend in the luminescence intensity has been reported in $ZnGa_2O_4$ and $ZnAl_2O_4$ [78,79]. However, the 730 nm emission band increased with the Fe^{3+} doping concentration, attaining maximum at 0.05 mol% of Fe^{3+} and decreased afterwards. The emission band observed at 487 nm in the $ZnAl_2O_4$ (x = 0) is assigned to the defect related intra-band transitions, such as oxygen vacancies and Zn^{2+} interstitials in the spinel lattice [2,80]. The quenching of the
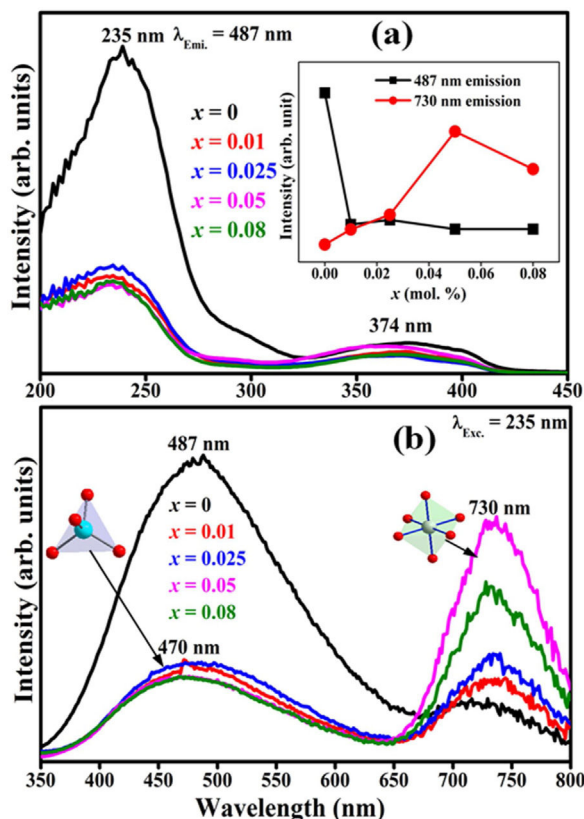
Fig. 13 – The PL (a) excitation (under 487 nm emission) and (b) emission (under 235 nm excitation) spectra of $ZnAl_{(2-x)}Fe_x^{3+}O_4$ ($x = 0, 0.01, 0.025, 0.05, 0.08$) phosphors normalized with respect to the dopant concentration. The inset of (a) shows the variation of the 487 and 730 nm bands as a function of Fe^{3+} concentration.
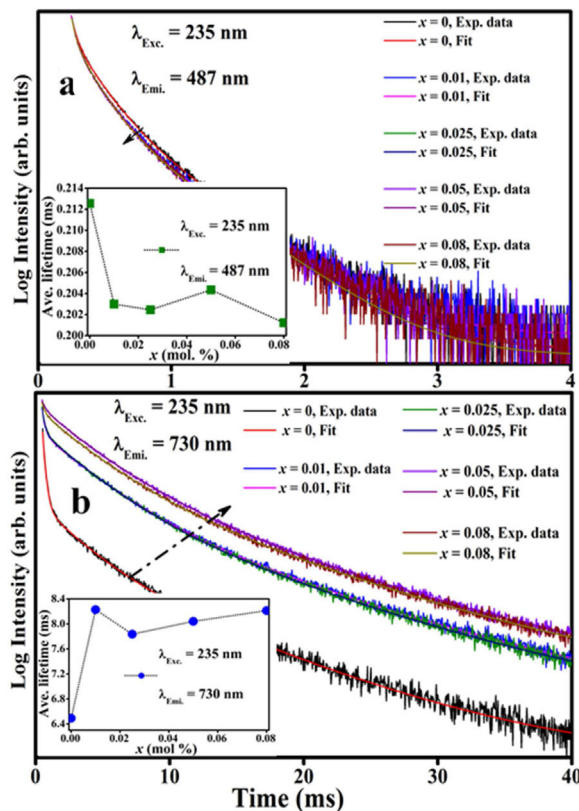

Fig. 14 – The decays curves for $ZnAl_{(2-x)}Fe_x^{3+}O_4$ ($x = 0, 0.01, 0.025, 0.05, 0.08$) phosphors when monitoring (a) 487 nm and (b) 730 nm emission under 235 nm excitation. The insets of (a) and (b) are the plot of the average lifetime of the phosphors versus the Fe^{3+} concentration (x) for the 487 nm emission and 730 nm emissions, respectively.

487 nm band on Fe^{3+} doping suggests that the introduction of Fe^{3+} into the $ZnAl_2O_4$ system must have decreased the oxygen vacancies and Zn interstitial sites [77], with Fe^{3+} filling some of the Zn interstitials. This will lead to the creation of some Fe–O–Fe bonds in the matrix and hence resulting in the formation of $ZnAl_{(2-x)}Fe_x^{3+}O_4$ composite. Contrary to the 487 nm bands, the emission intensities of the bands at 730 nm shows distinctive increment with Fe^{3+} concentration, with the highest emission intensity obtained from the samples with 0.05 mol% of Fe^{3+}. Observe the slight blue shift in the emission band maximum from 487 to 470 nm for the undoped and 0.08 mol Fe^{3+} doped sample. This indicates that these bands were not from the same origin. The emission bands at 470 and 730 nm in Fe^{3+} doped samples are ascribed to Fe ions occupying the tet and oct sites of $ZnAl_2O_4$ host, respectively. The PL from the tet coordinated Fe ions is attributed to the $^4E + ^4A_1(^4G) \rightarrow ^6A_1(^6S)$ transition, while the oct coordinated Fe ions is attributed to the $^4T_2(^4G) \rightarrow ^6A_1(^6S)$ [81]. As observed from the XPS result (Fig. 9(a)), part of the Fe^{3+} was reduced to Fe^{2+}, hence both the tet and the oct emission could be from a mixture of Fe^{2+} and Fe^{3+} ions.

The decay curves originating from the 487 and 730 nm emission under the 235 nm excitation of the $ZnAl_{(2-x)}Fe_x^{3+}O_4$ ($x = 0, 0.01, 0.025, 0.05, 0.08$) phosphors are shown in Fig. 14(a)

and (b), respectively. The decay curves were nicely fitted by a triple exponential equation given by Eq. (17):

$$I = \left[A\,exp\left(-\frac{t}{\tau_1}\right) + B\,exp\left(-\frac{t}{\tau_2}\right) + \left(-\frac{t}{\tau_3}\right) \right] \qquad (17)$$
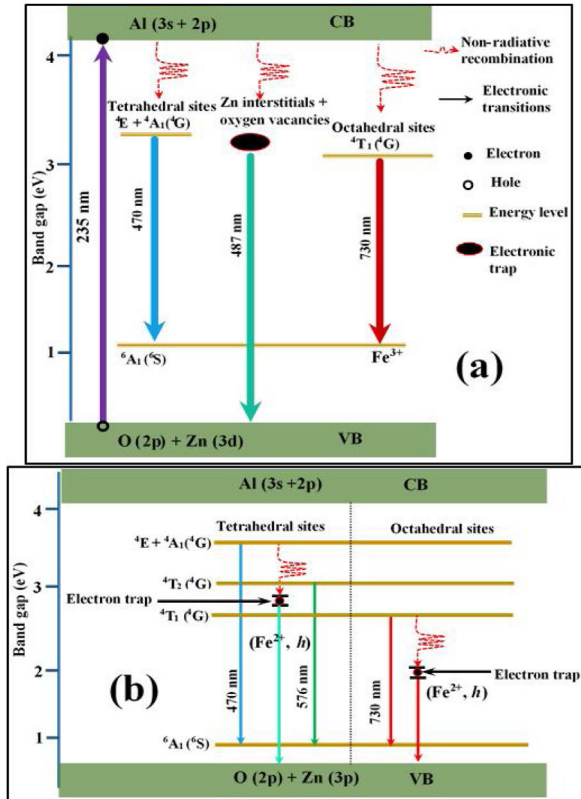
with I the PL intensity, A, B and C are the fitting parameters, while τ_1, τ_2 and τ_3 are the decay constants of the exponential components [82]. The average decay time τ^* can be determined using Eq. (18):

$$\tau^* = \frac{A\tau_1^2 + B\tau_2^2 + C\tau_3^2}{A\tau_1 + B\tau_2 + C\tau_3} \qquad (18)$$

The calculated average decay times for the 487 and 730 nm emission bands under 235 nm excitation are shown in Table 6. The inset of Fig. 14(a) shows the plot of the average lifetime of the phosphors versus the Fe^{3+} concentration (x) for the 487 nm emission under 235 nm excitation. The undoped sample (i.e. $ZnAl_2O_4$) has the longest lifetime, after which there was a decrease in the lifetime upon Fe^{3+} doping. The lifetime measured from the 730 nm emission when under the 235 nm excitation showed similar behavior like the one observed from the 487 nm, but in an opposite manner. As seen in the inset of Fig. 14(b), the undoped sample has the shortest lifetime,
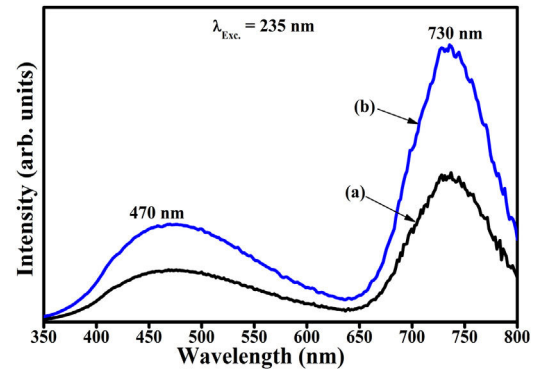
Table 6 – The average lifetime of $ZnAl_{(2-x)}Fe_x^{3+}O_4$ ($x = 0$, 0.01, 0.025, 0.05 and 0.08) for 487 and 730 nm emissions, when monitoring the excitation at 235 nm.

$ZnAl_{(2-x)}Fe_x^{3+}O_4$	Average lifetime (ms), $\lambda_{Exc.} = 235\,nm$	
	$\lambda_{Emi.} = 487\,nm$	$\lambda_{Emi.} = 730\,nm$
$x = 0$	0.21(3)	6.4(9)
$x = 0.01$	0.20(3)	8.2(3)
$x = 0.025$	0.20(2)	7.8(4)
$x = 0.05$	0.20(4)	8.0(4)
$x = 0.08$	0.20(1)	8.2(1)

Fig. 16 – The PL emission spectra of (a) $Zn_{(1-x)}Fe_x^{3+}Al_2O_4$ and (b) $ZnAl_{(2-x)}Fe_x^{3+}O_4$ for $x = 0.05$, excited at 235 nm.

Fig. 15 – Schematic energy diagrams showing, (a) the emission of Fe, zinc interstitials and oxygen vacancies in $ZnAl_2O_4$ host and (b) the electronic transitions Fe ions (Fe^{3+} and Fe^{2+}) on the tet and the oct sites of $ZnAl_2O_4$ host.

and the lifetime increased upon Fe^{3+} doping. The change in the lifetime upon Fe^{3+} doping is a demonstration of that the emissions arises from different lattice sites [83]. This is a further proof of the existence of the tet and oct Fe sites within the $ZnAl_{(2-x)}Fe_x^{3+}O_4$ matrix.

Fig. 15(a) is a schematic energy diagram showing the emission of Fe, zinc interstitials and oxygen vacancies in $ZnAl_2O_4$ host. The valence (VB) band is formed by the hybridization of O^{2-} 2p orbitals and Zn^{2+} 3d orbitals, while the conduction band (CB) is formed by Al 3s and 2p orbitals [4,84,85]. Upon excitation at 235 nm UV-light, electrons excited from the VB to the CB are relaxed non-radiatively to the various luminescent centers in the material before giving emissions. Since the combination of $ZnAl_2O_4$ and Fe_3O_4 gives a solid solution of the form, $(Zn_{8-x}^{2+}Fe_x^{3+})_{tet}[Al_{8-x}^{3+}Fe_x^{3+}Fe_8^{2+}]_{oct}O_{32}$, with Fe ions in

the both sites. The implication of this is that part of the Fe^{3+} are reduce to Fe^{2+} in both tet and oct sites. Therefore, the Fe emission from the tet and oct comprises Fe^{3+} and Fe^{2+} emissions. Fig. 15(b) illustrates further the schematic energy diagram of Fe ions (Fe^{3+} and Fe^{2+}) on the tet and the oct sites of $ZnAl_2O_4$ host. The Fe^{2+} ions were generated due to the photoionization Fe^{3+} that results to the formation of bound-hole state via the equation: $Fe^{3+} + h\nu \rightarrow [Fe^{2+}, h]$ [86]. The tet site is composed of two emission lines at 470 and 576 nm assigned to the $^4E + {}^4A_1(^4G) \rightarrow {}^6A_1(^6S)$ and $^4T_2(^4G) \rightarrow {}^6A_1(^6S)$ transitions of Fe^{3+}, respectively, while the oct site gave an emission line at 730 nm $(^4T_1(^4G) \rightarrow {}^6A_1(^6S))$ [81]. The recombination of the trapped electrons (bound-hole state) in the tet and oct sites has not been for $ZnAl_2O_2:Fe^{3+}$. However, it has been reported around 693 and 844 nm for the oct and tet sites in Fe_3O_4 (inverse spinel) [87], respectively.

Fig. 16(a) and (b) compares the PL spectra of $Zn_{(1-x)}Fe_x^{3+}Al_2O_4$ and $ZnAl_{(2-x)}Fe_x^{3+}O_4$ ($x = 0.05$, i.e. $Zn_{(0.95)}Fe_{0.05}^{3+}Al_2O_4$ and $ZnAl_{(1.95)}Fe_{0.05}^{3+}O_4$), respectively, taking into account the influence of charge compensation. It is evident from Fig. 16 that the PL intensity of the sample where Fe^{3+} substituted Al^{3+} (Fig. 16(b)) is about twice that of the sample where Fe^{3+} substituted Zn^{2+} (Fig. 16(a)). The decreased luminescence intensity in Fig. 16(b) is attributed to the charge imbalance in the matrix due to the substitution of divalent Zn^{2+} ion by trivalent Fe^{3+} ion. Charge imbalance can lead to the formation of charge defects in the host lattice and hence creating non-radiative luminescence centers in the material [17].

Fig. 17 shows CL spectra of $ZnAl_{(2-x)}Fe_x^{3+}O_4$ ($x = 0$, 0.01, 0.025, 0.05, 0.08). Generally, the wavelengths of the CL peak maximum shifted with respect to the PL peaks. The peak maximum observed at 487 nm in the PL result shifted to 503 nm for the undoped sample and 486 nm for the doped samples, while the PL maximum observed at 730 nm shifted to 703 nm. The shift observed in the wavelength maximum of the CL spectra compared to the PL spectra could be relate to the different excitation sources used to excite the samples in both cases. During PL, the charge carriers are excited using photons, while the charge carriers in CL are excited using high-energy electrons. CL can provide a better spatial resolution than PL, this can be correlated to the small beam diameter (<10 nm) of the electron beam [88]. Similar to the PL spectra (Fig. 13(a)), the band
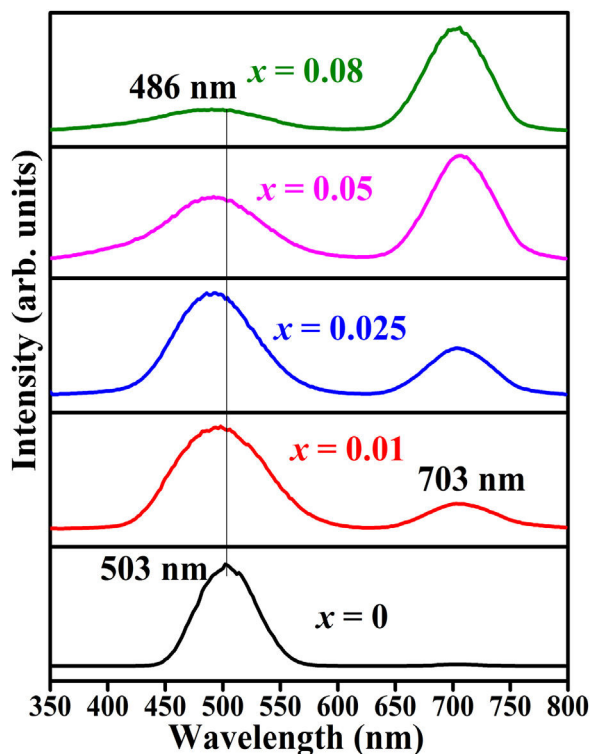
Fig. 17 – The CL spectra of ZnAl$_{(2-x)}$Fe$_x^{3+}$O$_4$ (x = 0, 0.01, 0.025, 0.05, 0.08) phosphors.

maximum observed at 503 nm in the undoped sample shifts to lower wavelength with increasing Fe^{3+} concentration, but the 703 nm peak remain at the similar position.

Conclusion

The Pechini synthesis method has proven to be an easy route to prepare ZnAl$_2$O$_4$ doped Fe^{3+} phosphors. The XRD results confirmed that the phosphors crystallized at a very low annealing temperature (600 °C). The crystallite sizes estimated from the XRD data were smaller than the grain size estimated from the FE-SEM micrograph due to the formation of poly-crystalline aggregates in the FE-SEM micrograph. The oxygen parameter (u) and the inversion degrees (y) of the phosphors were estimated from the XRD data. The XPS results confirmed the presence of Fe ions in both the tet and oct sites of ZnAl$_2$O$_4$. Furthermore, the XPS data also confirmed that Fe^{2+} ions were present in the samples doped with Fe^{3+}, suggesting the reduction of some of the Fe^{3+} ions to Fe^{2+} ions. From the diffuse reflectance data, the band gaps of the phosphors estimated using the Kubelka–Munk equation and the derivative method gave similar values. In agreement with the XPS result, the PL and the CL study of the phosphors showed two broad bands at around 470 and 730 nm which were assigned to the $^4E + {}^4A_1(^4G) \rightarrow {}^6A_1(^6S)$ and $^4T_2(^4G) \rightarrow {}^6A_1(^6S)$ electronic transitions of Fe^{3+} ions occupying the tet and the oct sites in the spinel ZnAl$_2$O$_4$ host, respectively.

REFERENCES

[1] E. Rusu, V. Ursak, G. Novitschi, M. Vasile, P. Petrenco, L. Kulyuk, Luminescence properties of ZnGa$_2$O$_4$ and ZnAl$_2$O$_4$ spinels doped with Eu^{3+} and Tb^{3+} ions, Phys. Stat. Solidi C 6 (2009) 1199–1202.

[2] N. Pathak, S.K. Gupta, K. Sanyal, M. Kumar, R.M. Kadama, V. Natarajan, Photoluminescence and EPR studies on Fe^{3+} doped ZnAl$_2$O$_4$: an evidence for local site swapping of Fe^{3+} and formation of inverse and normal phase, Dalton Trans. 43 (2014) 9313–9323.

[3] N. Kashii, H. Maekawa, Y. Hina, Dynamics of the cation mixing of MgAl$_2$O$_4$ and ZnAl$_2$O$_4$ spinel, J. Am. Ceram. Soc. 82 (1999) 1844–1848.

[4] K.E. Sickafus, J.M. Wills, N.W. Grimes, Structure of spinel, J. Am. Ceram. Soc. 82 (1999) 3279–3292.

[5] C.S. Hartley, Materials science for the experimental mechanist, in: W.N. Sharpe Jr. (Ed.), Springer Handbook of Experimental Solid Mechanics, Springer Science+Business Media, LLC New York, 2008, p. 25.

[6] V.V. Ursaki, I.M. Tiginyanu, Relation of A^{II}B^{III}$_2$X^{VI}$_4$ compounds to other materials their properties and applications, in: F.J. Manjon, I. Tiginyanu, V. Ursaki (Eds.), Pressure-induced Phase Transitions in AB$_2$X$_4$ Chalcogenide Compounds, Springer-Verlag Berlin Heidelberg, 2014, pp. 1–50.

[7] C. Aprea, A. Greco, A. Maiorino, C. Masselli, A comparison between rare earth and transition metals working as magnetic materials in an AMR refrigerator in the room temperature range, Appl. Therm. Eng. 91 (2015) 767–777.

[8] H. Takahashi, H. Takahashi, K. Watanabe, H. Kominami, K. Hara, Y. Matsushima, Fe^{3+} red phosphors based on lithium aluminates and an aluminum lithium oxyfluoride prepared from LiF as the Li source, J. Lumin. 182 (2017) 53–58.

[9] J. Cui, L. Wang, Q. Shi, Y. Tian, P. Huang, C. Cui, Color-tunable luminescence and energy transfer of Eu^{2+}/Mn^{2+} co-doped Sr$_9$Lu(PO$_4$)$_7$ phosphors for white LEDs, Polyhedron 141 (2018) 284–288.

[10] L. Marciniak, K. Trejgis, Luminescence lifetime thermometry with Mn^{3+}–Mn^{4+} co-doped nanocrystals, J. Mater. Chem. C 6 (2018) 7092–7100.

[11] M. Hughes, J.E. Aronson, W.S. Brocklesby, D.P. Shepherd, D.W.R.J. Hewak, R.J. Curry, Transition metal-doped chalcogenide glasses for broadband near-infrared sources, in: A.C.J.A.C. Terry, W.A. Clarkson (Eds.), Solid State Laser Technologies and Femtosecond Phenomena, SPIE, vol. 5620, 2004, pp. 289–296.

[12] R. Moncorgé, Laser materials based on transition metal ions, Opt. Mater. 63 (2017) 105–117.

[13] C. Lin, L. Li, S. Dai, C. Liu, Z. Zhao, C. Bocker, C. Rüssel, Oxyfluoride glass-ceramics for transition metal Ion based photonics: broadband near-IR luminescence of nickel ion dopant and nanocrystallization mechanism, J. Phys. Chem. C 120 (2016) 4556–4563.

[14] S. Kück, Laser-related spectroscopy of ion-doped crystals for tunable solid-state lasers, Appl. Phys. B 72 (2001) 515–562.

[15] L.P. Sosman, A. López, S.S. Pedro, A.R.R. Papa, Photoluminescence of the

$Mg_2Al_4Si_5O_{18}$–Al_2O_3–$MgAl_2O_4$–SiO_2 ceramic system containing Fe^{3+} and Cr^{3+} as impurity ions, Opt. Mater. 76 (2018) 353–358.

[16] E. Malguth, A. Hoffmann, M.R. Phillips, Fe in III–V and II–VI semiconductors, Phys. Stat. Sol. (b) 245 (2008) 455–480.

[17] J. Liu, Z.C. Wu, P. Wang, Y.M. Mei, M. Jiang, S.P. Kuang, The effects of charge compensation on photoluminescence properties of a new green-emitting ZnB_2O_4:Tb^{3+} phosphor, Luminescence 29 (2014) 868–871.

[18] B. Guzelturk, P.L.H. Martinez, Q. Zhang, Q. Xiong, H. Sun, X.W. Sun, A.O. Govorov, H.V. Demir, Excitonics of semiconductor quantum dots and wires for lighting and displays, Laser Photon. Rev. 8 (2014) 73–93.

[19] J. Liu, H. Lian, C. Shi, Improved optical photoluminescence by charge compensation in the phosphor system $CaMoO_4$:Eu^{3+}, Opt. Mater. 29 (2007) 1591–1594.

[20] S. Shi, J. Gao, J. Zhou, Effects of charge compensation on the luminescence behaviour of Eu^{3+} activated $CaWO_4$ phosphor, Opt. Mater. 30 (2008) 1616–1620.

[21] M. Chen, Z. Xia, Q. Liu, Improved optical photoluminescence by charge compensation and luminescence tuning in $Ca_6Ba(PO_4)_4O$:Ce^{3+}, Eu^{2+} phosphors, Cryst. Eng. Comm. 17 (2015) 8632–8638.

[22] P. Kumari, Y.D. wivedi, Structural and photophysical investigations of bright yellow emitting Dy: $ZnAl_2O_4$ nanophosphor, J. Lumin. 178 (2016) 407–413.

[23] B.S. Ravikumar, H. Nagabhushana, S.C. Sharma, B.M. Nagabhushana, Low temperature synthesis, structural and dosimetric characterization of $ZnAl_2O_4$:Ce^{3+} nanophosphor, Spectrochim. Acta Part A 122 (2014) 489–498.

[24] P.M. Shirage, A.K. Rana, Y. Kumar, S. Sen, S.G. Leonardi, G. Neri, Sr- and Ni-doping in ZnO nanorods synthesized by a simple wet chemical method as excellent materials for CO and CO_2 gas sensing, RSC Adv. 6 (2016) 82733–82742.

[25] A.K. Rana, P. Bankar, Y. Kumar, M.A. More, D.J. Late, P.M. Shirage, Synthesis of Ni-doped ZnO nanostructures by low temperature wet chemical method and their enhanced field emission properties, RSC Adv. 6 (2016) 104318–104324.

[26] R.D. Shannon, Acta Crystallogr., Sect. A: Cryst. Phys., Diffr. Theor. Gen. Cryst. 32 (1976) 751.

[27] G.K. Williamson, W.H. Hall, X-ray line broadening from filed aluminium and wolfram, Acta Metall. 1 (1953) 22–31.

[28] V.D. Mote, Y. Purushotham, B.N. Dole, Williamson–Hall analysis in estimation of lattice strain in nanometer-sized ZnO particles, J. Theor. Appl. Phys. 6 (2012) 6–13.

[29] Y. Waseda, E. Matsubara, K. Shinoda, X-ray Diffraction Crystallography, Springer-Verlag Berlin Heidelberg, 2011, pp. 75.

[30] J.W. Graydon, D.W. Kirk, The evidence for a miscibility gap in the Fe_3O_4–$ZnFe_2O_4$ system – a review, Mater. Trans. B 19 (1988) 919–925.

[31] J.R. Hill, R.J. Craig, G.V. Gibbs, Systematics of the spinel structure type, Phys. Chem. Miner. 4 (1979) 317–339.

[32] S. Ferrari, R.S. Kumar, F. Grinblat, J.C. Aphesteguy, F.D. Saccone, D. Errandonea, In-situ high-pressure X-ray diffraction study of zinc ferrite nanoparticles, Solid State Sci. 56 (2016) 68–72.

[33] G. Zhang, H. Dong, H. Jiang, R.K. Kukkadapu, J. Kim, D. Eberl, Z. Xu, Biomineralization associated with microbial reduction of Fe^{3+} and oxidation of Fe^{2+} in solid minerals, Am. Mineral. 94 (2009) 1049–1058.

[34] V.P. Lemos, M.L. da Costa, R.L. Lemos, M.S.G. de Faria, Vivianite and siderite in lateritic iron crust: an example of bioreduction, Quim. Nova 30 (2007) 36–40.

[35] F. Bosi, G.B. Andreozzi, U. Hålenius, H. skogby, Zn–O tetrahedral bond length variations in normal spinel oxides, Am. Miner. 96 (2011) 594–598.

[36] I.B. Villamil, S. Gallego, Charge order at magnetite Fe_3O_4(0 0 1): surface and Verwey phase transitions, J. Phys. Condens. Matter 27 (2015) 012001–012008.

[37] T. Ferreira, W. Rasband, ImageJ User Guide, 2012, http://imagej.nih.gov/ij/docs/guide.

[38] W.N. Wang, W. Widiyastuti, T. Ogi, I.W. Lenggoro, K. Okuyama, Correlations between crystallite/particle size and photoluminescence properties of submicrometer phosphors, Chem. Mater. 19 (2007) 1723–1730.

[39] Q. Li, C.W. Kartikowati, S. Horie, T. Ogi, T. Iwaki, K. Okuyama, Correlation between particle size/domain structure and magnetic properties of highly crystalline Fe_3O_4 nanoparticles, Sci. Rep. 7 (2017) 9894–98911.

[40] R.K. Tamrakar, D.P. Bisen, I.P. Sahu, K. Upadhyay, M. Sahu, Structural characterization of Gd_2O_3 phosphor synthesized by solid state reaction and combustion method using X-ray diffraction and transmission electron microscopic techniques, J. Display Technol. 12 (2016) 921–927.

[41] C. Suryanarayana, Mechanical Alloying and Milling, Marcel Dekker, NY, 2014, pp. 333.

[42] F. Adams, Chemical imaging analysis, in: C. Barbante (Ed.), Comprehensive Analytical Chemistry, vol. 69, Elsevier B.V., Radarweg Amsterdam, Netherlands, 2015, pp. 269–313.

[43] Royal Society of Chemistry, X-ray photoelectron spectroscopy, https://www.rsc.org/publishing/journals/prospect/ontology.asp?id=CMO:0000404&MSID=B602486F (May 2019).

[44] Operator's PHI MULTIPAK Software Manual, Version 8.2C, Ulvac-PHI, Inc., Chigasaki City, Kanagawa Prefecture, Japan, 2007.

[45] S.S. Pitale, V. Kumar, I.M. Nagpure, O.M. Ntwaeaborwa, H.C. Swart, Luminescence characterization and electron beam induced chemical changes on the surface of $ZnAl_2O_4$:Mn nanocrystalline phosphor, Appl. Surf. Sci. 257 (2011) 3298–3306.

[46] G. Cabello, L. Lillo, C. Caro, M. Seguel, C. Sandoval, G.E. Buono-Core, B. Chornik, M. Flores, A photochemical proposal for the preparation of $ZnAl_2O_4$ and $MgAl_2O_4$ thin films from beta-diketonate complex precursors, Mater. Res. Bull. 77 (2016) 212–220.

[47] K.G. Tshabalala, I.M. Nagpure, H.C. Swart, O.M. Ntwaeaborwa, S.-H. Cho, J.-K. Park, Enhanced green emission from UV down-converting Ce^{3+}–Tb^{3+} co-activated $ZnAl_2O_4$ phosphor, J. Vac. Sci. Technol. B 30 (2012) 031401–031407.

[48] M.S. Amer, M.A. Ghanem, A.M. Al-Mayouf, P. Arunachalam, Low-symmetry mesoporous titanium dioxide (lsm-TiO_2) electrocatalyst for efficient and durable oxygen evolution in aqueous alkali, J. Electrochem. Soc. 165 (2018) H300–H309.

[49] K.G. Tshabalala, S.-H. Cho, J.-K. Park, S.S. Pitale, I.M. Nagpure, R.E. Kroon, H.C. Swart, O.M. Ntwaeaborwa, Luminescent properties and X-ray photoelectron spectroscopy study of $ZnAl_2O_4$:Ce^{3+},Tb^{3+} phosphor, J. Alloys Compd. 509 (2011) 10115–10120.

[50] D.A. Pawlak, K. Wozniak, Z. Frukacz, T.L. Barr, D. Fiorentino, S. Seal, ESCA studies of yttrium aluminum garnets, J. Phys. Chem. B 103 (1999) 1454–1461.

[51] C. Fei, H. Liu, X. Wang, X. Fan, The influence of process parameters and pulse ratio of precursors on the characteristics of $La_{1-x}Al_xO_3$ films deposited by atomic layer deposition, Nanoscale Res. Lett. 10 (2015) 180–189.

[52] D.B. Chung, H.Y. Kim, M. Jeon, D.H. Lee, H.S. Park, S.H. Choi, S.W. Nam, S.C. Jang, J.-H. Park, K.-Y. Lee, C.W. Yoon, Enhanced ammonia dehydrogenation over Ru/La(x)–Al_2O_3 ($x = 0$–50 mol%): structural and electronic effects of La doping, Int. J. Hydrogen Energy 42 (2017) 1639–1647.

[53] X. Li, J. Zhang, M. Zhang, W. Zhang, M. Zhang, H. Xie, Y. Wu, Y. Tan, The support effects on the direct conversion of

syngas to higher alcohol synthesis over copper-based catalysts, Catalysts 9 (2019) 199–2016.

[54] M. Alizadeh, H. Mehdipour, V. Ganesh, A.N. Ameera, B.T. Goh, A. Shuhaimi, S.A. Rahman, Plasma-assisted hot filament chemical vapor deposition of AlN thin films on ZnO buffer layer: toward highly c-axis-oriented, uniform, insulative films, Appl. Phys. A 117 (2014) 2217–2224.

[55] T. Wang, H. Lei, Novel polyelectrolyte–Al_2O_3/SiO_2 composite nanoabrasives for improved chemical mechanical polishing (CMP) of sapphire, J. Mater. Res. 34 (2019) 1073–1082.

[56] P. Reinke, Inorganic Nanostructures, Wiley-VCH Verlag & Co. KGaA, Weinheim, Germany, 2012, pp. 41.

[57] M. Usman, M. Arshad, S.S. Suvanam, A. Hallén, Influence of annealing environment on the ALD-Al_2O_3/4H–SiC interface, J. Phys. D: Appl. Phys. 51 (2018) 105111–105127.

[58] T. Helmenstine, List of electronegativity values of the elements, https://sciencenotes.org/list-of-electronegativity-values-of-the-elements/ (June 2019).

[59] D. Zhang, Q. Guo, Y. Ren, C. Wang, Q. Shi, Q. Wang, X. Xiao, W. Wang, Q. Fan, Influence of inversion defects and Cr–Cr pairs on the photoluminescent performance of $ZnAl_2O_4$ crystals, J. Sol–Gel Sci. Technol. 85 (2018) 121–131.

[60] S. Yngman, S.R. McKibbin, J.V. Knutsson, A. Troian, F. Yang, M.H. Magnusson, L. Samuelson, R. Timm, A. Mikkelsen, Surface smoothing and native oxide suppression on Zn doped aerotaxy GaAs nanowires, J. Appl. Phys. 125 (2019) 025303–0253011.

[61] N. Li, L. Zhang, J. Zhou, D. Jing, Y. Sun, Localized nano-solid-solution induced by Cu doping in ZnS for efficient solar hydrogen generation, Dalton Trans. 43 (2014) 11533–11541.

[62] J.J. Beltrán, C.A. Barrero, A. Punnoose, Relationship between ferromagnetism and formation of complex carbon bonds in carbon doped ZnO powders, Phys. Chem. Chem. Phys. 21 (2019) 8808–8819.

[63] D. Zhang, C. Du, J. Chen, Q. Shi, Q. Wang, S. Li, W. Wang, X. Yan, Q. Fan, Improvement of structural and optical properties of $ZnAl_2O_4$:Cr^{3+} ceramics with surface modification by using various concentrations of zinc acetate, J. Sol–Gel Sci. Technol. 88 (2018) 422–429.

[64] S. Karamata, R.S. Rawat, P. Lee, T.L. Tan, R.V. Ramanujan, Structural, elemental, optical and magnetic study of Fe doped ZnO and impurity phase formation, Proc. Nat. Sci. Mater. 24 (2014) 142–149.

[65] K.O. Moura, R.J.S. Lima, A.A. Coelho, E.A. Souza-Junior, J.G.S. Duque, C.T. Meneses, Tuning the surface anisotropy in Fe-doped NiO nanoparticles, Nanoscale 6 (2014) 352–357.

[66] T. Yamashita, P. Hayes, Analysis of XPS spectra of Fe^{2+} and Fe^{3+} ions in oxide materials, Appl. Surf. Sci. 254 (2008) 2441–2449.

[67] G. Riveros, H. Gómez, R. Henríquez, R. Sshrebler, R. Córdova, R.E. Marotti, E.A. Dalchiele, Electrodeposition and characterization of ZnX (X = Se, Te) semiconductor thin films, Bol. Soc. Chil. Quím. 47 (2002) 411.

[68] J. Tauc (Ed.), The Optical Properties of Solids, Academic Press, New York, 1966.

[69] S.K. Sampath, D.G. Kanhere, R. Pandey, Electronic structure of spinel oxides: zinc aluminate and zinc gallate, J. Phys. Condens. Matter 11 (1999) 3635–3644.

[70] R. Khenata, M. Sahnoun, H. Baltachea, M. Rérat, A.H. Reshak, Y. Al-Douri, B. Bouhafs, Full-potential calculations of structural, elastic and electronic properties of $MgAl_2O_4$ and $ZnAl_2O_4$ compounds, Phys. Lett. A 344 (2005) 271–279.

[71] R.C. Sripriya, E.S. Arasi, J. Madhavan, V.A. Raj, Synthesis and characterization studies of $ZnFe_2O_4$ nanoparticles, MMSE 9 (2017) 13–17.

[72] I. Nurhasanah, Photodegradation of rhodamine B by using $ZnFe_2O_4$ nanoparticles synthesized through precipitation method, IOP Conf. Ser. Mater. Sci. Eng. 202 (2017) 012044.

[73] G. Kortum, Reflectance Spectroscopy, Springer-Verlag, New York, 1969, pp. 103–169.

[74] W.A. Harrison, J. Tersoff, Tight-binding theory of heterojunction band lineups and interface dipoles, J. Vac. Sci. Technol. B 4 (1986) 1068–1073.

[75] M. Bouguerra, M. Samah, M.A. Belkhir, A. Chergui, L. Gerbous, G. Novet, D. Chateigner, R. Madelon, Intense photoluminescence of slightly doped $ZnO–SiO_2$ matrix, Chem. Phys. Lett. 425 (2006) 77–81.

[76] S. Mathur, M. Veith, M. Haas, H. Shen, N. Lecerf, V. Huch, S. Hufner, R. Haberkorn, H.P. Beck, Single-source sol–gel synthesis of nanocrystalline $ZnAl_2O_4$: structural and optical properties, J. Am. Ceram. Soc. 84 (2001) 1921–1928.

[77] K. Thirunavukkarasu, T.M. Sankaranarayanan, A. Pandurangan, R.V. Shanthi, S. Sivasanker, The role of surface Zn^{2+} ions in the transesterification of vegetable oils over ZnO supported on Al_2O_3 and Fe_2O_3, Catal. Sci. Technol. 4 (2014) 851–860.

[78] K. Sakoda, M. Hirano, Formation of complete solid solutions, $Zn(Al_xGa_{1-x})_2O_4$ spinel nanocrystals via hydrothermal route, Ceram. Int. 40 (2014) 15841–15848.

[79] K. Sakoda, M. Hirano, Effect of heat-treatment and composition on structure and luminescence properties of spinel-type solid solution nanocrystals, J. Nanosci. Nanotechnol. 15 (2015) 6069–6077.

[80] L. Cornu, M. Gaudon, V. Juber, $ZnAl_2O_4$ as a potential sensor: variation of luminescence with thermal history, J. Mater. Chem. C 1 (2013) 5419–5428.

[81] S.S. Pedro, O. Nakamura, R.B. Barthem, L.P. Sosman, Photoluminescence and photoacoustic spectroscopies of Fe^{3+} in the $LiGa_5O_8–LiGaSiO_4–Li_5GaSi_2O_8$ system, J. Fluoresc. 19 (2009) 211–219.

[82] S. Chemingui, M. Ferhi, K. Horchani-Naifer, M. Ferid, Synthesis and luminescence characteristics of Dy^{3+} doped $KLa(PO_3)_4$, J. Lumin. 166 (2015) 82–87.

[83] M. Zhao, H. Liao, M.S. Molokeev, Y. Zhou, Q. Zhang, Q. Liu, Z. Xia, Emerging ultra-narrow-band cyan-emitting phosphor for white LEDs with enhanced color rendition, Light-Sci. Appl. 8 (2019) 38–47.

[84] M. Hughes, J.E. Aronson, W.S. Brocklesby, D.P. Shepherd, D.W. Hewak, R.J. Curry, Transition metal-doped chalcogenide glasses for broadband near-infrared sources, in: A.C.J.A.C. Terry, W.A. Clarkson (Eds.), Solid State Laser Technologies and Femtosecond Phenomena, vol. 5620, SPIE, 2004, pp. 289–296.

[85] E.O. Filatova, A.S. Konashuk, Interpretation of the changing the band gap of Al_2O_3 depending on its crystalline form: connection with different local symmetries, J. Phys. Chem. C 119 (2015) 20755–20761.

[86] K. Pressel, A. Dörnen, G. Rückert, Charge-transfer transitions and pseudoacceptor states of iron in gallium phosphide, Phys. Rev. B 47 (1993) 16267–16273.

[87] M.E. Sadat, M.K. Baghbador, A.W. Dunn, H.P. Wagner, R.C. Ewing, J. Zhang, H. Xu, G.M. Pauletti, D.B. Mast, D. Shi, Photoluminescence and photothermal effect of Fe_3O_4 nanoparticles for medical imaging and therapy, Appl. Phys. Lett. 105 (2014) 091903–091908.

[88] V. Piazza, L. Mancini, H.L. Chen, S. Collin, M. Tchernycheva, Nanoscale analyses applied to nanowire devices, in: S. Mokkapati, C. Jagadish (Eds.), Nanowires for Energy Applications (Semiconductors and Semimetals), vol. 98, Academic Press, Cambridge, USA, 2018, pp. 231–319.